Monthly Notices
of the
ROYAL ASTRONOMICAL SOCIETY

MNRAS **480,** 2881–2897 (2018)
Advance Access publication 2018 August 2

doi:10.1093/mnras/sty1983

X-ray/UV/optical variability of NGC 4593 with *Swift*: reprocessing of X-rays by an extended reprocessor

I. M. McHardy,[1★] S. D. Connolly,[1] K. Horne,[2] E. M. Cackett,[3] J. Gelbord,[4] B. M. Peterson,[5,6] M. Pahari,[1,7] N. Gehrels,[8] M. Goad,[9] P. Lira,[10] P. Arevalo,[11] R. D. Baldi,[1] N. Brandt,[12] E. Breedt,[13] H. Chand,[14] G. Dewangan,[7] C. Done,[15] M. Elvis,[16] D. Emmanoulopoulos,[1] M. M. Fausnaugh,[5] S. Kaspi,[17] C. S. Kochanek,[5] K. Korista,[18] I. E. Papadakis,[19] A. R. Rao,[20] P. Uttley,[21] M. Vestergaard[22,23] and M. J. Ward[16]

Affiliations are listed at the end of the paper

Accepted 2018 July 23. Received 2018 July 18; in original form 2017 December 12

ABSTRACT

We report the results of intensive X-ray, UV, and optical monitoring of the Seyfert 1 galaxy NGC 4593 with *Swift*. There is no intrinsic flux-related spectral change in any variable component with small apparent variations being due to contamination by a constant hard (reflection) component in the X-rays and the red host galaxy in the UV/optical. Relative to the shortest wavelength band, *UVW*2, the lags of the other UV/optical bands mostly agree with the predictions of reprocessing of high energy emission by an accretion disc. The *U*-band lag is, however, larger than expected, probably because of reprocessed Balmer continuum emission from the distant broad line region (BLR). The *UVW*2 band is well correlated with the X-rays but lags by $\sim$6$\times$ more than expected if the *UVW*2 results only from reprocessing of X-rays by the disc. However, if the light curves are filtered to remove variations on time-scales $>$5 d, the lag approaches the expectation from disc reprocessing. MEMECHO analysis shows that direct X-rays can be the driver of most of the UV/optical variations if the response functions have tails up to 10 d, from BLR reprocessing, together with strong peaks at short lag ($<$1 d) from disc reprocessing. For the 5 AGN monitored so far, the observed *UVW*2 to *V*-band lags are $\lesssim$2 of disc reprocessing expectations and vary little between AGN. However, the X-ray to *UVW*2 lags greatly exceed disc reprocessing expectations and differ between AGN. The two most absorbed AGN have the largest excesses, so absorption and scattering may affect these lags, but there is no simple relationship between excess and absorption.

Key words: galaxies: active – galaxies: individual: NGC 4593 – galaxies: Seyfert – ultraviolet: galaxies – X-rays: galaxies.

1 INTRODUCTION

The origin of the UV and optical variability in AGN, and its relationship to the X-ray variability, are questions of major relevance to understanding the central structures of AGN. One possible explanation of UV/optical variability is that variations in the thermal emission from the accretion disc are caused by fluctuations in the inward accretion flow (Arévalo & Uttley 2006). A second possibility is that X-ray emission from the central corona or very hard UV emission from the very inner edge of the accretion disc illuminates the outer disc, heating it up and causing it to re-radiate (Haardt & Maraschi 1991).

The time lag between the high energy emission and the re-radiated lower energy UV/optical emission gives us the distance between these two emission regions. Therefore, by measuring the lags between the high energy emission and a number of UV/optical bands we can map out the temperature structure of the disc. This technique is known as 'reverberation mapping' (RM; Blandford & McKee 1982) and has been used to map regions too small to be resolved by direct imaging, e.g. AGN broad line regions (BLR; Peterson 2014).

The model of a smooth, optically thick, geometrically thin, efficiently radiating accretion disc was first derived by Shakura & Sunyaev (1973, SS) and has been our basic disc model for over

★ E-mail: imh@soton.ac.uk

40 yr. In this model, the release of gravitational potential energy from accreting material leads to a temperature profile (in physical units) of $T(R) \propto R^{-3/4}(M\dot{m})^{1/4}$. Incident high energy emission will enhance the existing thermal emission (slightly altering the disc temperature profile). We thus expect a wavelength (λ) dependent lag, τ, between the incident high energy, and re-radiated UV/optical emission, of $\tau = R/c \propto (M^2\dot{m}_E)^{1/3}\lambda^{\beta}$ where $\beta = 4/3$ and $\dot{m}_E$ is the accretion rate in Eddington units (Cackett, Horne & Winkler 2007). We also expect the optical variations to be smoother and have lower amplitude of variability than the UV variations as they will come from a larger emission region. Both Cackett et al. (2007) and Sergeev et al. (2006) find lags consistent with $\beta = 4/3$ between various optical bands. However neither study included X-ray data.

A number of observers have studied the relationship between the X-ray and UV or optical wavebands, mostly combining ground-based optical observations with space-based X-ray observations from *RXTE* (e.g. Uttley et al. 2003; Suganuma et al. 2006; Arévalo et al. 2008, 2009; Breedt et al. 2010; Lira et al. 2011; Cameron et al. 2012). These observations have mostly shown strong X-ray/optical correlations on short time-scales (weeks–months), with the optical lagging the X-rays by ∼1 d, but have sometimes shown long-term trends (months–years) in the optical which are not mirrored in the X-rays (e.g. Breedt et al. 2009). There are occasional examples where the UV/optical appears to lead the X-rays on short time-scales, in particular in NGC 7469 (Nandra et al. 1998) where although the dips in the 30 d *RXTE* X-ray and *IUE* 1315 Å UV light curve line up with approximately zero lag, the best-defined peak in the UV light curve is 4d before an X-ray peak. There is almost certainly more than one cause of the UV/optical variability with long time-scale variations probably being dominated by accretion rate fluctuations propagating inwards through the disc. Interpretation of the origin of the short time-scale variations depends very much on whether the X-rays lead or lag the UV/optical emission. Although, overall, the observations from the sample of AGN monitored by *RXTE* strongly support the conclusion that the optical lags the X-rays, in no individual case is the uncertainty on the lag small enough to be absolutely sure that the optical does lag.

Recent monitoring campaigns with *Swift* (e.g. McHardy et al. 2014; Shappee et al. 2014; Edelson et al. 2015; Fausnaugh et al. 2016; Troyer et al. 2016; Edelson et al. 2017) have greatly improved the measurement of lags between the X-ray, UV, and optical bands and have therefore significantly improved our understanding of the origin of UV/optical variability in AGN. However, these observations have also highlighted questions about the structures of accretion discs, of the importance of the BLR in producing reprocessed UV and optical emission and about whether X-rays from the central corona or maybe hard UV emission from the inner edge of the accretion disc are driving the longer wavelength UV/optical variability. The above campaigns all show that the longer wavelength *Swift* UVOT bands lag behind the shortest wavelength *Swift* UV band (*UVW2*; 193 nm) in a manner which is in agreement with the short time-scale (weeks/months) UV/optical variability of AGN being produced by reprocessing of radiation of shorter wavelength than *UVW2* and coming from a compact region near the black hole. However, McHardy et al. (2014) noted that if all of the reprocessing is being carried out by a surrounding accretion disc, that the disc is either hotter than or larger than we should expect, assuming the SS model and given the mass and accretion rate of the target AGN. All subsequent papers (e.g. Fausnaugh et al. 2016) found a similar result. These observations were consistent with microlensing observations (e.g. Dai et al. 2010; Morgan et al. 2010; Mosquera et al. 2013) which had already pointed out a similar disc size discrepancy. It was also clear (e.g. Edelson et al. 2015; Fausnaugh et al. 2016) that the lag in the *u* band was longer than that in surrounding bands, indicating that the BLR was also contributing to the lags.

There has additionally been the concern that the optical light curves do not look as expected if they arise from reprocessing of X-ray emission from a small central corona, e.g. of size similar to that which we measure from microlensing observations, i.e. $\lesssim 10R_G$ (Dai et al. 2010; Mosquera et al. 2013), or from X-ray low/high energy reverberation, i.e. $\sim 4R_g$ (Cackett et al. 2014; Emmanoulopoulos et al. 2014). The observed optical light curves are smoother than expected and an insufficient fraction of the X-ray emission hits the disc to power the optical variability (e.g. Berkley, Kazanas & Ozik 2000; Arévalo et al. 2008). Larger coronal sizes are required. Gaskell (2008) also notes the energetics problem and proposes variations originating independently in different parts of the disc. However, although such a model is useful for explaining the uncorrelated variations between bands which are sometimes seen, it cannot explain the well correlated multiwavelength variations seen in the *Swift* observations. Gardner & Done (2017) proposed an alternative model in which the X-ray emission does not directly impact on the outer disc but mainly heats up the very inner edge of the disc, which then inflates and re-radiates at hard UV wavelengths on to the outer disc. In this model there should be an additional lag between the X-ray and *UVW2* emission, over and above that expected from an extrapolation of the longer wavelength lags down to the X-ray waveband. This additional lag would correspond to the thermal time-scale for the incident X-ray heating to pass through the inner disc to the re-radiation surface. Gardner & Done (2017) note the existence of such a lag when the unfiltered X-ray and *UVW2* observations of NGC 5548 are compared. However, McHardy et al. (2014) do not see any additional lag in NGC 5548 if those light curves are filtered to remove variations on time-scales longer than 20 d. In NGC 4151, Edelson et al. (2017) see a very large excess lag between the X-ray and *UVW2* bands. Unlike in NGC 5548, the excess lag in NGC 4151 is strongly energy dependent, with the highest energy X-rays having the largest lag. NGC 4151 is the most absorbed of the few AGN whose lags have been well studied so far and so the energy dependence may be a function of scattering in the absorbing medium.

So far the number of AGN with accurately measured lags is small. With *Swift*, lags have been measured well in NGC 5548 (McHardy et al. 2014; Edelson et al. 2015; Fausnaugh et al. 2016) and NGC 4151 (Edelson et al. 2017) and less thoroughly in NGC 2617 (Shappee et al. 2014) and NGC 6814 (Troyer et al. 2016). With *XMM–Newton* lags have been measured in NGC 4395 between the X-ray and one UV (*UVW1*) and one optical (*g*) band (McHardy et al. 2016). NGC 4593 has a black hole mass which is almost an order of magnitude lower than that of the other AGN for which multiband monitoring has been performed by *Swift*. Thus, in 20 d of *Swift* observations we can probe relative size scales (measured in gravitational radii) which would require monitoring, although at reduced frequency, over a few months for the other AGN. We also note that the AGN in which lags have been measured well so far have been of relatively low accretion rate (NGC 4395 $\dot{m}_E \sim 0.0012$, NGC 4151 $\dot{m}_E \sim 0.021$, NGC 5548 $\dot{m}_E \sim 0.048$). We therefore proposed for *Swift* monitoring of the somewhat higher accretion rate NGC 4593 ($\dot{m}_E \sim 0.081$), allowing us to investigate the importance of accretion rate and disc temperature in determining disc and BLR structure.

In Section 2, we present the *Swift* observations and light curves. The X-ray spectrum is relevant to understanding of lags and disc structure as, in the model of Gardner & Done (2017), the tail of a

luminous hard UV emission component may be expected to show up in at low X-ray energies. Thus, in Section 3, we discuss the time average *Swift* X-ray spectrum and X-ray spectral variability. In Section 4, we discuss the relationships, and lags, between the X-ray and the various UV/optical bands. In Section 5, we compare the lags and the observed *UVW2* light curve with the predictions from reprocessing of X-rays by a simple SS accretion disc. In Section 6, we present a more sophisticated maximum entropy modelling of the X-ray/UV/optical light curves to derive reprocessing functions which are more complex than that expected from a simple accretion disc and which indicate the importance of reprocessing from the BLR. This topic is addressed in detail in a paper by Cackett et al. (2018) based on parallel *Hubble Space Telescope* (*HST*) observations of NGC 4593. In Section 7, we compare the present lag measurements of NGC 4593 with those of other AGN and note broadly similar (scaled) lags between the UV and optical bands but differences in the X-ray/UV lags. We draw some brief conclusions regarding the inner structure of AGN.

Just before submission of this paper, the *Swift* data from this programme were published by another group (Pal & Naik 2018). Although there are some similarities, their analysis and conclusions differ from ours in a number of respects, as we shall note below.

2 *SWIFT* OBSERVATIONS

Swift observed NGC 4593 almost every orbit (96 min) for 6.4 d from 2016 July 13 to 18 and thereafter every second orbit for a further 16.2 d. Each observation totalled approximately 1 ks although observations were often split into two, or sometimes more, visits. The *Swift* X-ray observations are made by the X-ray Telescope (XRT; Burrows et al. 2005) and UV and optical observations are made by the UV and Optical Telescope (UVOT; Roming et al. 2005). In total 194 visits satisfying standard good time criteria, such as rejecting data when the source was located on known bad pixels (e.g. see https://swift.gsfc.nasa.gov/analysis/xrt_swguide_v1_2.pdf), were made. The XRT observations were carried out in photon-counting (PC) mode and the UVOT observations were carried out in image mode. X-ray light curves in a variety of energy bands were produced using our own Southampton pipeline which is based upon the standard *Swift* analysis tasks as described in Cameron et al. (2012). We made flux measurements for each visit thus providing the best available time resolution. In addition, for comparison, a broad-band 'snapshot' X-ray light curve (i.e. one flux point per visit) was produced using the Leicester Swift Analysis system (Evans et al. 2007), which was almost identical to our own snapshot light curve. X-ray data are corrected for the effects of vignetting and aperture losses and data with large flux error (>0.15 count s^{-1}) are rejected.

During each X-ray observation, measurements were made in all six UVOT filters, using the 0x30ed mode which provides exposure ratios, for the *UVW2*, *UVM2*, *UVW1*, *U*, *B*, and *V* bands, of 4:3:2:1:1:1. UVOT light curves with the same time resolution were made using the Southampton system and also, independently, using a system developed by Gelbord & Edelson (2017). The latter system includes a detailed comparison of UVOT 'drop out' regions, as first discussed in observations of NGC 5548 (Edelson et al. 2015). When the target source is located in such regions the *UVW2* count rate is typically 10–15per cent lower than in other parts of the detector. The drop in count rate is energy dependent, being greatest in the *UVW2* band and least in the *V* band. The new drop-out box regions are based on intensive *Swift* observations of three AGN, i.e. NGC 5548 (Edelson et al. 2015), NGC 4151 (Edelson et al. 2017), and the present observations of NGC 4593. Observations falling in drop-out regions were rejected. We also searched for observations where the fluxes in the six UVOT bands showed a particularly red spectral slope. Such observations almost always fell within a drop-out region and were also rejected.

The resultant light curves are shown in Fig. 1. We see a close correspondence between all UVOT bands and a reasonable correspondence between the X-ray and UVOT bands. In Fig. 1 we also show the X-ray hardness. The correspondences between these light curves are discussed in the following sections.

3 X-RAY SPECTRUM AND VARIABILITY

3.1 Time averaged X-ray spectrum

The X-ray spectrum can provide information which is relevant to understanding the inner geometries of AGN and so we have fitted models with XSPEC to the *Swift* XRT time averaged spectrum derived from the observations shown in Fig. 1. The 2–8 keV spectrum is fitted well by a simple power law, with line-of-sight Galactic column cold hydrogen absorber of 1.89×10^{20} cm^{-2}, together with a broad Gaussian line at 6.4 and a narrow line at ∼7 keV. The photon index of the power law is $\Gamma = 1.68 \pm 0.02$. When this model is extended down to 0.3 keV a large negative residual is seen centred on ∼1 keV which is consistent with the presence of warm absorbers as detected by previous observers using data from *XMM–Newton* (Brenneman et al. 2007) and combined data from *XMM–Newton* and NuStar (Ursini et al. 2016b). Following these studies we add two warm absorbers which results in a good fit to the 0.3–8 keV spectrum with $\Gamma = 1.74 \pm 0.01$. This fit is similar to that of Brenneman et al ($\Gamma = 1.75^{+0.02}_{-0.03}$) except that, unlike them, we do not require an additional 'soft-excess' component at low energies.

NGC 4593 is detected in the *Swift* BAT 70 month survey (Baumgartner et al. 2013). The spectrum is described as a power law with $\Gamma = 1.84^{+0.07}_{-0.08}$ and flux (14–195 keV) of $8.8 \pm 0.05 \times 10^{-11}$ erg cm^{-2} s^{-1} (https://swift.gsfc.nasa.gov/results/bs70mon/SWIFT_J1239.6-0519). During the monitoring reported here the average 0.3–10 keV flux was $\sim 4.5 \times 10^{-11}$ erg cm^{-2} s^{-1}. To extrapolate a power law to the BAT energy band, and obtain the observed BAT flux requires $\Gamma = 1.73$, indicating that the long-term average X-ray luminosity of NGC 4593 has not changed noticeably. Including the BAT data into our spectral fit without any change of normalization, and assuming a simple power law without any high energy cut-off, steepens the overall fit slightly ($\Gamma = 1.82^{+0.04}_{-0.05}$). The overall best fit is shown in Fig. 2 and the fit parameters are given in Table 1.

To the best-fitting model we added, separately, a bremsstrahlung (zbremss) and a Comptonization (comptt) component as used by Brenneman et al. (2007) to describe a soft excess which they find in their *XMM–Newton* data. In our *Swift* data the normalizations of both components are consistent with zero and the 1σ upper limit on the 0.3–10 keV fluxes for these two components are 6×10^{-16} and 3.4×10^{-17} erg cm^{-2} s^{-1}, respectively (compared to 2×10^{-14} and 6.46×10^{-14} erg cm^{-2} s^{-1}, respectively, from Brenneman et al.). We note that Brenneman et al. find variation in the soft excess between different observations so it is possible that we observed with *Swift* when the soft excess was particularly faint. Pal & Naik (2018) present a 0.3–7 keV *Swift* XRT spectrum. It is of much lower S/N than that presented here, possibly being only from a single 1 ks observation. They are therefore able only to fit to a power law, whose slope is not well constrained, and a blackbody. They do not include the warm absorbers or the iron lines.

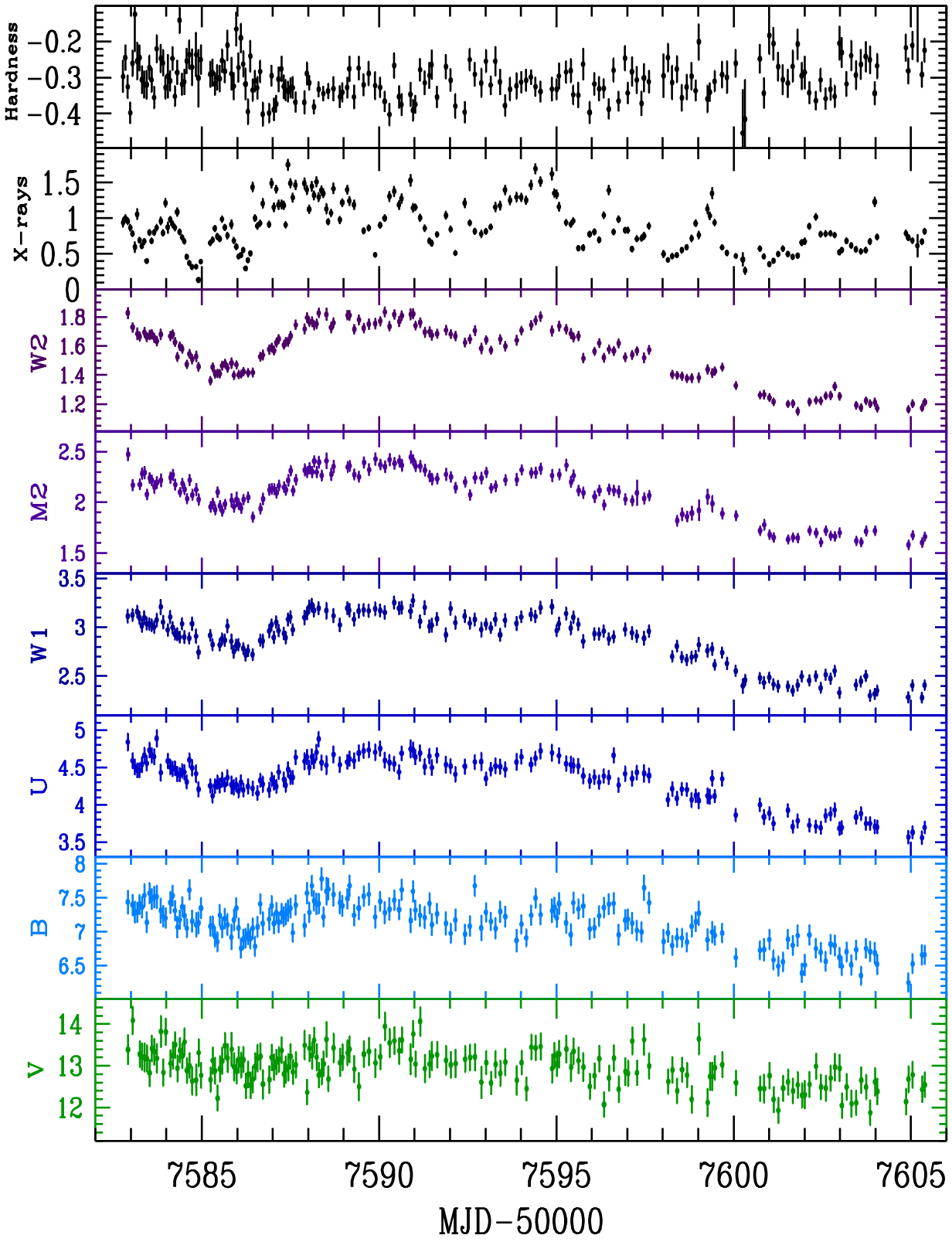

Figure 1. XRT and UVOT light curves of NGC 4593. The top panel is the hardness ratio defined as $H-S/H+S$ where H is the 2–10 keV count rate and S is the 0.5–2 keV count rate. The second from top panel is the 0.5–10 keV count rate for each visit. The lower panels are the *UVW*2 through to *V*-band fluxes in units of mJy.

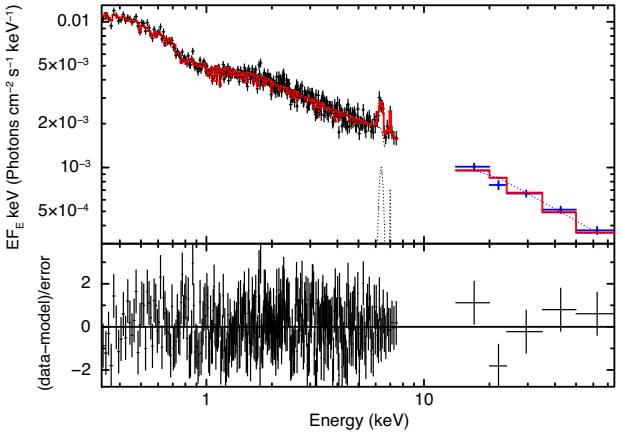

Figure 2. Best fit, with residuals, to the time averaged XRT and BAT spectrum. The fit parameters are given in Table 1.

Table 1. X-ray spectral fit parameters.

Spectral parameters	Fitted values
$N_{H,\mathrm{tbabs}}$ (10^{22} cm^{-2})	0.0189 (f)
$NH_{\mathrm{WA1,zxipcf}}$ (10^{22} cm^{-2})	$1.22^{+0.12}_{-0.13}$
$\log \zeta_{\mathrm{WA1,zxipcf}}$	$0.87^{+0.11}_{-0.12}$
$f_{\mathrm{WA1,zxipcf}}$	$0.47^{+0.02}_{-0.03}$
$NH_{\mathrm{WA2,zxipcf}}$ (10^{22} cm^{-2})	$33.9^{+7.8}_{-12.3}$
$\log \zeta_{\mathrm{WA2,zxipcf}}$	$3.51^{+0.03}_{-0.02}$
$f_{\mathrm{WA2,zxipcf}}$	1 (f)
$\Gamma_{\mathrm{zpowerlw}}$	$1.82^{+0.04}_{-0.05}$
F_{zpowerlw} (10^{-11} erg s^{-1} cm^{-2})	$4.73^{+0.05}_{-0.08}$
$E_{\mathrm{K}\alpha,\mathrm{zgauss}}$ (keV)	$6.42^{+0.03}_{-0.04}$
$\sigma_{\mathrm{K}\alpha,\mathrm{zgauss}}$ (keV)	$0.21^{+0.04}_{-0.06}$
$F_{\mathrm{K}\alpha,\mathrm{zgauss}}$ (10^{-11} erg s^{-1} cm^{-2})	$0.072^{+0.013}_{-0.024}$
$Q_{\mathrm{K}\alpha,\mathrm{zgauss}}$ (eV)	373^{+63}_{-57}
$E_{\mathrm{K}\beta,\mathrm{zgauss}}$ (keV)	$7.06^{+0.07}_{-0.08}$
$\sigma_{\mathrm{K}\beta,\mathrm{zgauss}}$ (keV)	0.05 (f)
$F_{\mathrm{K}\beta,\mathrm{zgauss}}$ (10^{-11} erg s^{-1} cm^{-2})	$0.023^{+0.014}_{-0.008}$
$Q_{\mathrm{K}\beta,\mathrm{zgauss}}$ (eV)	86^{+40}_{-39}
$F_{0.3-2}$ (10^{-11} erg s^{-1} cm^{-2})	$1.39^{+0.05}_{-0.04}$
F_{2-10} (10^{-11} erg s^{-1} cm^{-2})	$3.43^{+0.04}_{-0.03}$
F_{10-100} (10^{-11} erg s^{-1} cm^{-2})	$5.52^{+0.06}_{-0.11}$
χ^2/dof	374/342

Best-fitting model parameters from the simultaneous fitting of *Swift*/XRT and *Swift*/BAT energy spectra using the model CONST × TBABS × [ZXIPCF*ZXIPCF*ZPOWERLW+ZGAUSS+ZGAUSS]. $N_{H,\mathrm{tbabs}}$ is the Galactic absorption column density, $NH_{\mathrm{WA1,zxipcf}}$, $\log \zeta_{\mathrm{WA1,zxipcf}}$, and $f_{\mathrm{WA1,zxipcf}}$ are the column density, ionization parameter, and partial covering fraction, respectively, due to the first warm absorber component while the same parameters for the second warm absorber component are denoted by 'WA2'. $\Gamma_{\mathrm{zpowerlw}}$ is the photon power-law index. $E_{\mathrm{K}\alpha,\mathrm{zgauss}}$, $\sigma_{\mathrm{K}\alpha,\mathrm{zgauss}}$, and $Q_{\mathrm{K}\alpha,\mathrm{zgauss}}$ denote the line energy, line width, and the equivalent width of the Fe Kα emission line while $E_{\mathrm{K}\alpha,\mathrm{zgauss}}$, $\sigma_{\mathrm{K}\alpha,\mathrm{zgauss}}$, and $Q_{\mathrm{K}\alpha,\mathrm{zgauss}}$ denote the line energy, line width, and the equivalent width of the Fe Kβ emission line, respectively. F_{zpowerlw}, $F_{\mathrm{K}\alpha,\mathrm{zgauss}}$, and $F_{\mathrm{K}\beta,\mathrm{zgauss}}$, F_{cutoffpl} are the fluxes due to ZPOWERLW and two ZGAUSS models, respectively, in the energy range 0.3–10.0 keV. $F_{0.3-2.0}$, $F_{2.0-10.0}$, $F_{10.0-100.0}$ are unabsorbed fluxes in the energy range 0.3–2 keV, 2–10 keV, and 10–100 keV, respectively.

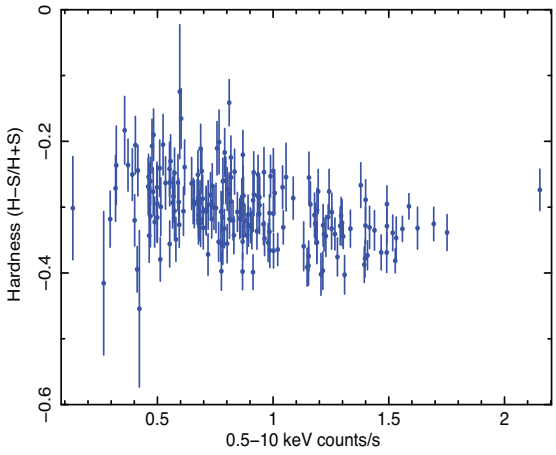

Figure 3. The X-ray hardness as a function of the 0.5–10 keV count rate. The hardness is defined as $(H-S)/(H+S)$, where S = 0.5–2 keV and H = 2–10 keV count rate.

3.2 X-ray spectral variability and X-ray energy dependence of lags

In *Swift* observations of NGC 4151, Edelson et al. (2017) found large differences in the lag measured between different X-ray bands and the *UVW2* band. Although M$^{\mathrm{c}}$Hardy et al. (2014) did not find any significant differences between the 0.5–2 keV versus *UVW2* lags and the 2–10 keV versus *UVW2* lags in NGC 5548, the possibility exists that different X-ray bands may come from different locations and so give rise to different lags.

We have therefore made light curves in a variety of narrow and broad X-ray energy bands and have searched for lags between them using a variety of techniques. We can find no measureable lags. For example, using JAVELIN (Zu, Kochanek & Peterson 2011; Zu et al. 2013), we find that the 0.5–2keV band lags the 2–10 keV band by $-0.001^{+0.003}_{-0.004}$ d. Similarly the lag of the 2–10 keV band by the 0.3–1 keV band is $-0.002^{+0.004}_{0.005}$ d.

As an additional method of searching for differences between X-ray bands we have calculated the hardness ratio. The hardness ratio is defined as $(H-S)/(H+S)$, where here the hard (H) band is 2–10 keV and the soft (S) band is 0.5–2 keV. We plot this ratio as a function of time in the top panel of Fig. 1. There is little variation. In Fig. 3, we plot the hardness ratio against broad-band (0.5–10 keV) count rate. Above 0.5 counts s^{-1} there is a very slight softening of the spectrum with increasing count rate. This spectral softening is similar to that found in NGC 4593 by Ursini et al. (2016a) and for AGN in general by Sobolewska & Papadakis (2009). Although they use 0.3–1.5 and 1.5–10 keV as their soft and hard band, respectively, and define hardness ratio as H/S rather than the $(H-S)/(H+S)$ used here, similar results are shown by Pal & Naik (2018).

We note here that below 0.5 counts s^{-1} (0.5–10 keV) data are limited so it is not clear whether the suggestion of softening with decreasing count rate, at the lowest count rates, is real or not. A softening with decreasing count rate at the lowest count rates has been seen in NGC 1365 (Connolly, M$^{\mathrm{c}}$Hardy & Dwelly 2014) and attributed to unabsorbed (i.e. steep spectrum) X-rays scattered from an accretion disc wind which are still visible even when the direct X-ray emission is heavily absorbed.

To determine whether the slight softening with increasing luminosity represents a real change in the underlying spectrum we plot, in Fig. 4, the 0.3–1 keV count rate against the 2–5 keV count rate. Similar flux–flux plots have been used elsewhere to investigate the

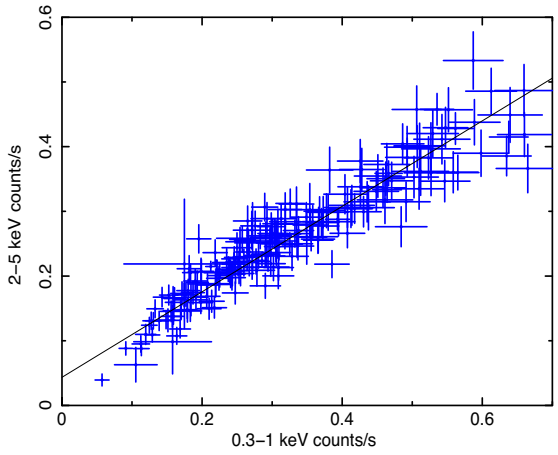

Figure 4. The 0.3–1 keV count rate plotted against the 2–5 keV count rate.

reasons behind flux-related X-ray spectral variations (e.g. Taylor, Uttley & McHardy 2003). Above a 0.3–1 keV count rate of ∼0.15 counts s^{-1}, there is a strong linear relationship between the count rates in the two bands with an extrapolation to zero 0.3–1 keV count rate giving a small residual count rate in the harder band. The data are again insufficient to determine whether there is any real deviation from this relationship at the very lowest count rates.

Five combined *XMM–Newton* and NuStar observations have been fitted with a multicomponent model including a power law and a high energy cut-off. From this modelling it is stated that the photon index varies by ∼0.25 over a factor 3 in luminosity (Ursini et al. 2016b). The NuStar observations extend to a higher energy than the *Swift* XRT observations but, within the XRT observations, the strong linear relationship between the hard and soft X-ray count rates shows that there is no change of spectral shape of the varying component as a function of luminosity over the large majority of the flux range observed. The weak softening of the overall spectrum with increasing luminosity shown in Fig. 3 is most simply explained as the combination of a small constant component of hard spectrum together with a varying soft spectrum component. The hard component may be a reflection component from the disc or BLR. We therefore conclude that, unlike in NGC 4151, all of the XRT energy band varies simultaneously and so, to increase S/N, we hereafter use the 0.5–10 keV band unless stated otherwise.

4 X-RAY/UV-OPTICAL CORRELATIONS

4.1 X-ray/*UVW2* discrete correlation function

Visual inspection of the X-ray and *UVW2* light curves indicates that most of the X-ray flux variations on ∼day time-scales have counterparts, though of lesser fractional variability (Table 2), in the *UVW2* light curve. As a basic method of quantifying the relationship between these two bands we show, in Fig. 5, the discrete correlation function (DCF; Edelson & Krolik 1988) between these two bands together with simulation-based confidence contours. We see that a correlation exists between these two bands at greater than 99 per cent confidence. This degree of confidence between the observed X-ray and *UVW2* light curves, without any filtering to remove long-term trends which often distort DCFs, is higher than in all other previous intensive *Swift* AGN monitoring programs (e.g. McHardy et al. 2014; Edelson et al. 2015, 2017). The peak lag corresponds to the *UVW2* lagging the X-rays by about half a day. The exact value of the lag will be considered in more detail later.

The confidence contours are calculated in broadly the same way as in our previous papers on X-ray/optical correlations (e.g. Breedt et al. 2009). X-ray light curves are simulated with the same variability properties, e.g. power spectral density (PSD) and count rate probability density function (PDF), as for the observed X-ray light curve. The N per cent confidence levels are defined such that if correlations are performed between the observed *UVW2* data and randomly simulated X-ray light curves, only $(100-N)$ per cent of the correlations would exceed those levels. The confidence levels are appropriate to a single trial, i.e. a search at zero lag, approximately what we are searching for here. For a search over a wide lag range where the expected lag was unknown, the confidence levels would be reduced by an amount depending on the ratio of the lag range being searched to the width of the expected correlation function (i.e. $(ACF\_Width_X^2 + ACF\_Width_O^2)^{1/2}$, where ACF_Width_X and ACF_Width_O are the half-widths of the X-ray and optical autocorrelation functions). If this ratio was R, then the single-trial confidence level of $(100-N)$ per cent would reduce to $(100-RN)$ per cent. We note that the previous light-curve simulation method depended only on the parameters of the X-ray PSD, using the method of Timmer & Koenig (1995). The present light-curve simulation method follows Emmanoulopoulos, McHardy & Papadakis (2013), with code available from Connolly (2015), which also takes account of the count rate PDF. Unlike the method of Timmer & Koenig (1995) which can only produce Gaussianly distributed light curves, this method can produce light curves with any PDF, including the highly non-linear light curves seen in the gamma-ray and TeV bands.

The level and detailed shape of the confidence contours do change, though only very slightly, depending on the model chosen for the X-ray PSD. Here, we used the standard bending power-law model of McHardy et al. (2004) with Poisson noise and fixed the low frequency PSD slope at −1. The PSD derived here from the *Swift* XRT observations is still not very well constrained but a high frequency slope of −1.8 was measured, similar to that (−2.2) found by Summons (2007) from *RXTE* and *XMM–Newton* observations. However, even quite large changes in the X-ray PSD model do not change the confidence contours greatly. In almost all tests the peak of the DCF reached a significance level of between ∼95 and 99 per cent.

DCFs for the relationship between the *UVW2* band and the other UVOT bands all show a strong peak near zero lag with very high significance (>99.9 per cent confidence) and are not shown here. The DCF does not provide a particularly accurate measurement of the value of the lag and so the lag measurements are derived using other methods, below.

4.2 X-ray/UV/optical interband lags

All lags are measured relative to the *UVW2* band as the *UVW2* band provides the highest significance detections of any of the UVOT bands. Lags, with errors, were measured both using JAVELIN (Zu et al. 2011, 2013), as previously demonstrated by Shappee et al. (2014), Pancoast, Brewer & Treu (2014), and McHardy et al. (2014) and using the 'flux randomization/random subset selection' (FR/RSS) method (Peterson et al. 1998) with the interpolation cross-correlation function (ICCF; Gaskell & Sparke 1986; Gaskell & Peterson 1987). The median lag values produced by JAVELIN are usually close to the values produced by the FR/RSS method but, as noted by Fausnaugh et al. (2016), the uncertainties are usually smaller,

Table 2. $F_{\rm var}$ and lags (d) relative to *UVW2* from various correlation methods.

Band	$F_{\rm var}$	JAVELIN	FR/RSS peak	FR/RSS centroid
0.5–10 keV	0.376	$-0.761^{+0.031}_{-0.030}$	-0.412 ± 0.186	-0.662 ± 0.145
UVW2	0.125	–	–	–
UVM2	0.110	$+0.038^{+0.037}_{-0.025}$	$+0.057 \pm 0.083$	$+0.069 \pm 0.086$
UVW1	0.092	$-0.013^{+0.034}_{-0.033}$	-0.013 ± 0.078	$+0.094 \pm 0.109$
U	0.070	$+0.275^{+0.042}_{-0.058}$	$+0.186 \pm 0.214$	$+0.317 \pm 0.127$
B	0.038	$+0.106^{0.134}_{-0.085}$	$+0.101 \pm 0.208$	$+0.191 \pm 0.175$
V	0.024	$+0.179^{0.177}_{-0.117}$	$+0.220 \pm 0.502$	$+0.247 \pm 0.386$

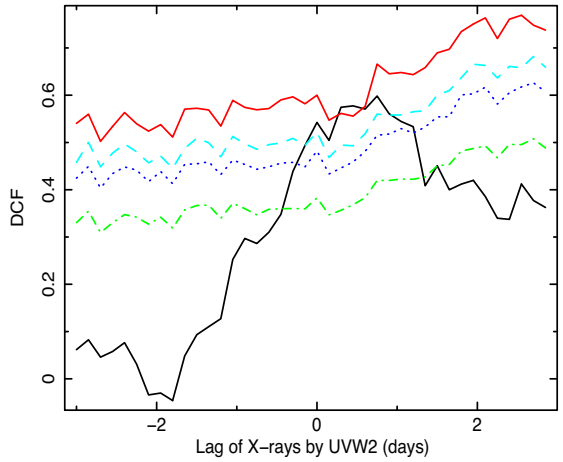

Figure 5. Solid black line–discrete cross-correlation function between the X-ray and *UVW2* light curves shown in Fig. 1. The 68 per cent (dot–dashed, green), 90 per cent (dotted, blue), 95 per cent (dashed turquoise), and 99 per cent (solid red) confidence levels are also shown.

here by a factor ∼3 (see Table 2). Detailed discussion of these differences is beyond the scope of this paper but will be included in a future *Swift* survey paper (Edelson et al., in preparation). There are other cross-correlations methods, e.g. the maximum interpolation interval CCF (MCCF) method (Oknyanskii 1993; Oknyansky et al. 2017) and the z-transformed DCF (ZDCF) method (Alexander 2013), which again usually produce similar results (e.g. M$^{\rm c}$Hardy et al. 2014).

The FR/RSS method produces two alternative lag measurements, based either on the distribution of the values of the centroids of the individual ICCFs (usually measured at 80 per cent of the peak value), or on the distribution of the peak lag values. With asymmetric ICCFs, these distribution will differ and provide us with different information. Where an ICCF arises from the sum of a number of contributing lags, the centroid provides us with an estimate of the average lag. The peak highlights the dominant contributor to the lags.

In Fig. 7, we show the lags measured, from the centroids of the FR/RSS lag distributions. We do not show the lags derived from the peaks of the FR/RSS distributions but we give the values in Table 2. In Fig. 8, we show the lags measured using JAVELIN which are more like the FR/RSS peak than centroid lags. The lag distributions between the *UVW2* and short wavelength bands (X-ray, *UVM2*) are symmetrical, but tails to longer lags appear in the *b* and *v* bands (Fig. 6) indicating a possible secondary source of lags.

Relative to *UVW2*, the other UV and optical band lags are very small. With all measurement methods we see that the *u*-band lag significantly exceeds any interpolation between the lags in bands on either side. As in NGC 5548 (Edelson et al. 2015; Fausnaugh et al. 2016), this excess lag is probably due to a contribution from the BLR as predicted by Korista & Goad (2001) and is discussed in detail for NGC 4593 by Cackett et al. (2018). The lag measured by JAVELIN to the *UVW1* band is actually negative, though is also consistent with a small positive value. Possibly there is some contribution from [C III] from the BLR to the emission in *UVW2* but not in *UVW1*.

Pal & Naik (2018), although finding lags which increase with wavelength, do not obtain the same lag values as those given here. The main difference between our analyses is that Pal and Naik use 1.5–10 keV as their reference band against which to measure lags in all other bands, from soft X-ray to *V* band, whereas we measure all other UVOT band lags relative to *UVW2*. As we see in Fig. 1, and as seen in all previous *Swift* AGN monitoring campaigns, the *UVW2* light curve has the highest S/N of any of the UVOT bands. Also the main change in the character of the variability is between the X-rays and *UVW2* whereas the other UVOT bands are quite similar in character to *UVW2*. Thus, the peak correlation strength between the X-rays and *UVW2* is ∼0.6 (as shown also by Pal and Naik) whereas the peak correlation strength between *UVW2* and the other UVOT bands is greater than 0.9. Thus, lag measurements between *UVW2* and the other UVOT bands have much smaller errors than lag measurements between the hard X-ray band and the UVOT bands. We also find no evidence for lags between hard and soft X-ray bands and so we measure a lag between *UVW2* and the broad 0.5–10 keV X-ray band, which has higher S/N than just the 1.5–10 keV band. Thus, we believe that the lags presented here are a more accurate measurement of the true lags than those presented by Pal and Naik.

In Figs 7 and 8, we also plot model lags on the assumption that the variable UV/optical emission is produced by reprocessing of X-ray emission by an accretion disc. To calculate these model lags we broadly follow Kazanas & Nayakshin (2001), Cackett et al. (2007), and Arévalo et al. (2008). We first assume that the steady-state temperature structure and emission from the disc, in the absence of X-ray illumination, is as given by Shakura & Sunyaev (1973). We then calculate the new temperature structure following X-ray illumination and hence derive the change in emission, in each *Swift* UVOT band, from every part of the disc. Taking account of the different light traveltimes from each part of the disc to the observer we add up the changes in emission as a function of time to produce the response functions, Fig. 9. As previously (e.g. M$^{\rm c}$Hardy et al. 2014), we take, as the model lag, the time for half of the reprocessed light to be received. We refer to this lag as the median lag.

There are a number of assumptions in the derivation of the response functions and in the resultant lag estimation which are discussed below (Section 5). Here we simply note that, if the model lags are measured relative to the *UVW2* band, then the other observed UV and optical lags agree reasonably with the model. This conclusion differs slightly from our conclusion regarding the lags

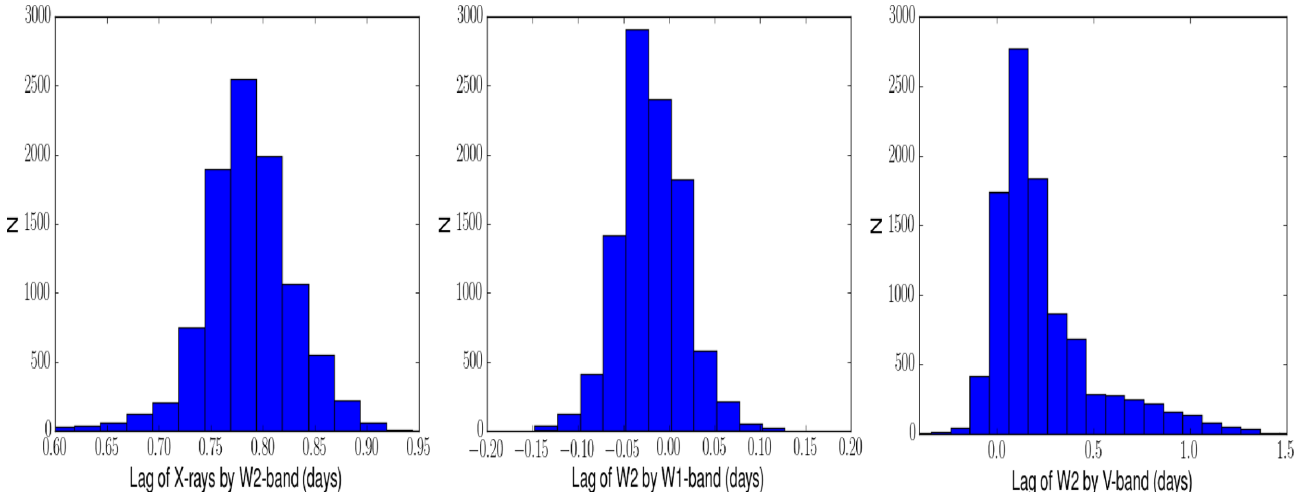

Figure 6. Lag probability distributions from JAVELIN for (left-hand panel) *UVW*2 relative to the X-rays, (centre) *UVW*1 relative to *UVW*2, and (right-hand pannel) *V* band relative to *UVW*2.

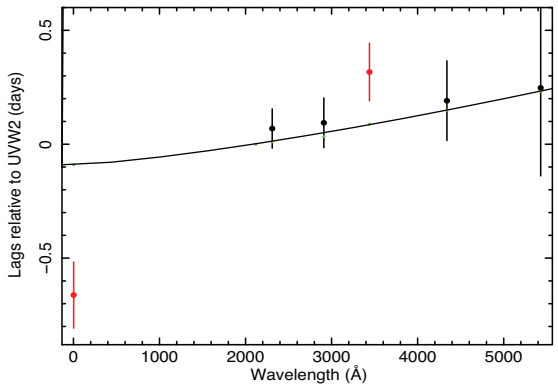

Figure 7. Lags relative to *UVW*2 derived from the centroids of the distribution using the FR/RSS method (Peterson et al. 1998). The thin line is a power-law fit with index 4/3 to the model lags (shown as small green dots). Here, the model lag is the time for half of the light to be received.

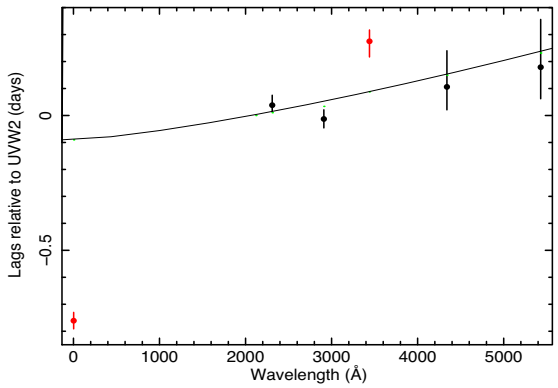

Figure 8. Lags relative to *UVW*2 derived using JAVELIN (Zu et al. 2011, 2013). The thin line is a power-law fit with index 4/3 to the model lags (shown as small green dots). Here, the model lag is the time for half of the light to be received.

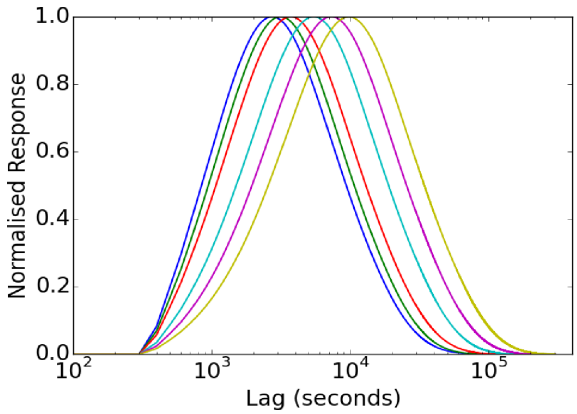

Figure 9. Impulse response functions, normalized to the peaks, for an accretion disc surrounding a Schwarzschild black hole of the mass of NGC 4593. It is assumed that the disc reaches to the last innermost stable circular orbit. The X-ray source is assumed to be a point source located 6 R_G above the axis of the black hole and we assume an inclination of 45°. The responses increase in lag through the UVOT bands from *UVW*2 to *V* band.

in NGC 5548 (McHardy et al. 2014) where, for the lag of the *UVW*2 band by the *V* band, we stated that the observed lags were a factor of 2.25 larger than the model. There is a slight caveat that the FORTRAN code which produced the model lags in McHardy et al. (2014) is no longer operational so a new PYTHON code was written which integrates the contributions from the different sections of the disc in a different way. The new code produces response functions which are very similar to the original code but the median lag time is ∼15−20 per cent longer. Given the complete independence of the two codes it is encouraging that they both produce very similar results. However, with the present code, we would have said that the observed *UVW*2-*V* band lag in NGC 5548 given in McHardy et al. (2014) was ∼1.9× longer than the model. We compare the *UVW*2-*V* band lags between different AGN in Section 7.

For either code, when we extrapolate the model back to the X-ray waveband, the observed *UVW*2 emission lags the X-rays by much more (factor ∼6) than expected from the model. Thus, although the lags within the UV and optical bands are quite consistent with reprocessing of far-UV emission by an accretion disc, as proposed

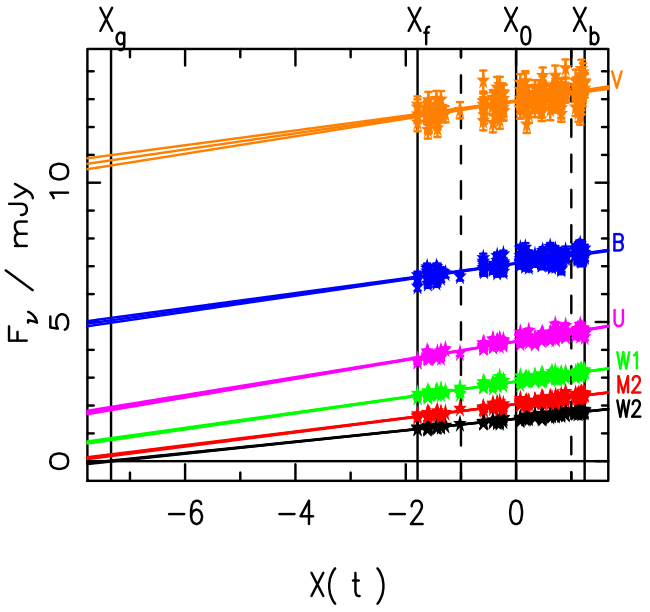

Figure 10. $F_\nu(\lambda, t)$ versus $X(t)$, as defined in equation (1), for each of the UVOT bands.

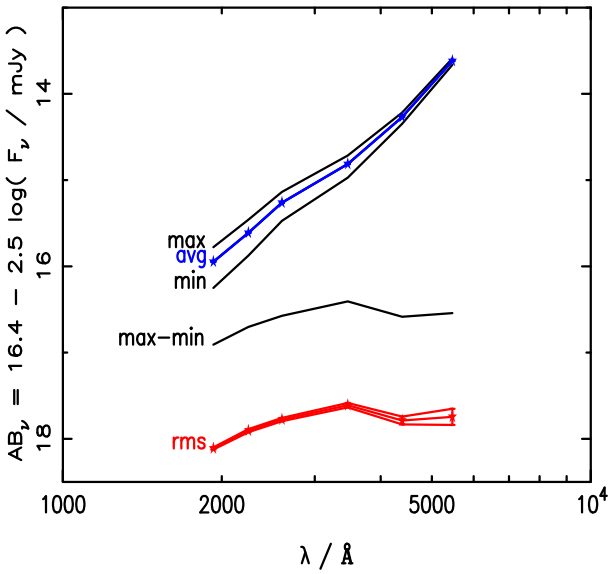

Figure 11. The lower curve, labelled 'rms', is the rms spectrum of the variable UVOT component, $R_\nu(\lambda)$, as defined in equation (1) and derived from the slopes of the plots shown in Fig. 10. The uncertainties are derived from the uncertainties on the slopes. The middle curve, labelled 'max–min', represents the difference between the maximum and minimum observed UVOT fluxes. The upper curve, labelled 'avg', is the lower limit on the constant host galaxy component of the UVOT fluxes, derived from the intercepts of the curves shown in Fig. 10 at the point where the *UVW2* flux is zero.

by Gardner & Done (2017), a simple lamp-post point X-ray source directly illuminating only a surrounding accretion disc cannot explain the complete spectrum of multiband lags from X-ray to *V* band. Possible explanations are discussed below (Sections 5 and 6).

4.3 UV-optical spectral variability

The light curves shown in Fig. 1, and the fractional variances listed in Table 2, show greater variability at shorter UVOT wavelengths. Is this difference a reflection of complex flux-related spectral variability or simply contamination by a galaxy component? We can investigate the origin of the variability using flux–flux analysis, similar to that employed above to investigate X-ray spectral variability.

Here, we fit the fluxes (here using F_ν in mJy) as a function of time, in each UVOT band, i.e. $F_\nu(\lambda, t)$, as

$$F_\nu(\lambda, t) = A_\nu(\lambda) + R_\nu(\lambda)X(t), \quad (1)$$

where $A_\nu(\lambda)$ is a constant component, representing the mean spectrum, $R_\nu(\lambda)$ is the rms spectrum, and $X(t)$ is a dimensionless light curve such that $\langle X\rangle = 0$ and $\langle X^2\rangle = 1$. In Fig. 10, we plot $F_\nu(\lambda, t)$ against $X(t)$ for each of the UVOT bands. A clear linear response is seen in all cases, together with different constant offsets. This linear response shows, as in the earlier X-ray flux–flux analysis, that each UVOT band is well described by a combination of a variable component whose spectrum does not change with luminosity, and a constant component. The 'bluer when brighter' variations that are apparent in the raw light curves are thus purely a result of dilution of a bluer variable component (from the accretion disc) and a redder component (from the host galaxy). Pal & Naik (2018) present plots of the raw UVOT count rates against the 1.5–10 keV count rate, showing approximate correlations with a good deal of scatter. They do not attempt any spectral modelling.

The slopes of $F_\nu(\lambda, t)$ versus $X(t)$ give R_ν, the spectrum of the variable component. This rms spectrum, with upper and lower limits derived from the slope uncertainties, is shown in Fig. 11. Also shown (max–min) is the spectral shape derived from the difference between the maximum and minimum observed UVOT fluxes. At $X(t) = -7.3$, the extrapolated *UVW2* flux is zero, which provides a lower limit on the contribution of the host galaxy. Together with the fluxes of all the other UVOT bands extrapolated to $X(t) = -7.3$ we can derive the spectrum of this contribution, shown by blue stars (avg) in Fig. 11. In Fig. 11, we can indeed see that the variable (disc) component is blue and the constant (host galaxy) component is red.

5 COMPARISON WITH SIMPLE ACCRETION DISC MODEL

To produce the impulse response functions shown in Fig. 9 we assumed an accretion disc as described by Shakura & Sunyaev (1973), surround a black hole with the mass and accretion rate of NGC 4593 as listed in Table 3. We assume an inclination of 45°. The choice of inclination does not have too great an effect on the median arrival time of reprocessed light but it has a very large effect on the time of the peak of the response. For an inclination of 45°, the peak of the response is a factor of ∼3 smaller than the median lag.

We assume a Schwarzschild black hole with an inner disc radius of 6 R_G. The exact value of the outer disc radius, assuming it is greater than a few hundred R_G, does not matter much. For a Kerr black hole with the disc again reaching to the innermost stable orbit, the median lag decreases by almost a factor 2. Thus, if all other disc parameters were well defined, lag measurement could, in principle, provide another method of black hole spin measurement, or at least of inner disc radius measurement. We assume illumination by a point X-ray source located 6 R_G above the axis of the black hole. We take the illuminating luminosity from the *Swift* BAT observations, extrapolating to 0.1–195 keV (Table 3). The albedo is not well known. It is probably high near the inner edge of the disc where the

Table 3. Black hole masses, accretion rates, and resultant accretion disc model lags between the X-ray and *UVW2* and between the *UVW2* and *V* bands. For NGC 4395 both the mass and the bolometric luminosity are from Peterson et al. (2005). The masses for NGC 4151, NGC 4593, and NGC 5548 are taken from Bentz & Katz (2015) and the bolometric luminosities used in the derivation of the accretion rates are the mean and spread of observations reported by Vasudevan & Fabian (2009), Vasudevan et al. (2009, 2010), and Woo & Urry (2002) The ionizing luminosity is taken from the BAT 70 month survey, extrapolated to 0.1–195 keV. Here, we assume an X-ray source height of $6R_g$, an inclination of 45°, an albedo of 0.8, and an inner disc radius of $6R_g$. The observed lags for NGC 4395 are from McHardy et al. (2016), for NGC 4151 from Edelson et al. (2017), for NGC 5548 from Edelson et al. (2015), for NGC 2617 from Fausnaugh et al. (2018), and the results for NGC 4593 are from this work. The lags measured by Fausnaugh et al. (2018) agree, within the errors, with those presented earlier by Shappee et al. (2014). For NGC 2617, the much higher S/N 5100 Å band rather than the very nearby *Swift V* band is used to measure the *UVW2-V* lag. In all cases, the lags are derived from the centroid distributions using the FR/RSS method and no long-term variations have been removed from any light curve. For NGC 4395 where the observed UV band was *UVW1*, the lag has been corrected to the *UVW2* band assuming a scaling with wavelength to a power 1.15, which is intermediate between the expected disc value of 1.333 and the value obtained by observation which, roughly, is close to unity. For NGC 4151 and NGC 5548, X-ray lags were derived from the X4 band. For NGC 4593 where there is no evidence of variation of lag with X-ray energy, the full 0.5–10 keV band is used, as it is for NGC 4395 where the source is too faint to measure lags relative to different energy bands. For NGC 2617, we take the mass, accretion rate, and bolometric luminosity from Fausnaugh et al. (2018). The ionizing luminosity is based on the discussion of the high energy X-ray luminosity in Shappee et al. (2014). However, we note that $L_{\rm ion}$ is not a critical parameter and increasing it by a factor of 3 increases the model lags by less than 1 per cent.

AGN	M 10^6 $M_\odot$	L_{Bol} 10^{43} erg s^{-1}	$\dot{m}_E$ %	L_{ion} 10^{43} erg s^{-1}	Model X-ray–*UVW2* lag (d)	Model *UVW2-V* lag (d)	Observed X-ray–*UVW2* lag (d)	Observed *UVW2-V* lag (d)
NGC 4151	37.6 ± 11.5	10 ± 5	2.1	2.6	0.174	0.425	$3.58^{+0.36}_{-0.46}$	$0.96^{+0.47}_{-0.46}$
NGC 4395	0.36 ± 0.11	0.0054	0.12	0.0016	0.00293	0.00748	$4.05^{+0.54}_{-1.13} \times 10^{-3}$	$5.07^{+0.74}_{-1.29} \times 10^{-3}$
NGC 4593	7.63 ± 0.16	7.8 ± 3.5	8.1	3.0	0.090	0.231	0.66 ± 0.15	0.247 ± 0.38
NGC 5548	52.3 ± 1.9	32 ± 20	4.8	10	0.286	0.698	1.12 ± 0.49	1.16 ± 0.53
NGC 2617	32.4^{+63}_{-21}	4.3 ± 0.4	1.0	1.0	0.125	0.300	$1.84^{+1.02}_{-0.94}$	$0.63^{+0.51}_{-0.48}$

surface of the disc may be ionized, but may be lower further out. Here, we assume an albedo of 0.8 but assuming an albedo of 0.2 only increases the median lag by 9 per cent.

We also consider only the variable component of the UV/optical emission, produced by reprocessing of high energy emission, rather than the total emission from the disc which would include emission produced by dissipation of gravitational potential energy from accreting material. As the illuminating high energy emission heats the disc, the reprocessed variable emission is associated with larger radii than the same wavelength of emission from the quiescent disc.

To determine how we should translate the response functions into predicted model lags we simulated a *UVW2* light curve with the observed X-ray light curve as input. Using the FR/RSS method the measured lag using the centroids of the correlation functions was 0.131 ± 0.024 and the lag using the peaks of the correlation functions was 0.076 ± 0.03. The model median lag from the response functions is 0.096, which corresponds reasonably to the measured lags. The arrival time of the peak of the response function is typically one-third of the median lag and so is much shorter than the measured lag. We therefore take the median lag of the response functions as our model lag.

5.1 Comparison of observed and model *UVW2* light curves: time-scale dependence of lags

Using our disc model, with parameters given above, we can simulate the expected *UVW2* light curve, assuming illumination of the disc by the observed X-ray light curve. The resulting model *UVW2* light curve and the observed *UVW2* light curve are shown in Fig. 12. Fluxes are not yet included precisely in the simulation code and so the model light curve has been arbitrarily normalized to the same mean as the observed light curve. A 'quiescent' level of 1 mJy, which is ∼0.2mJy below the lowest observed *UVW2* flux was removed from the *UVW2* light curve to highlight just the variable component.

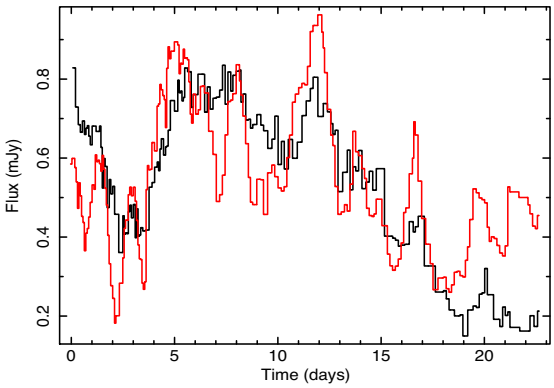

Figure 12. Observed *UVW2* light curve (black) with model *UVW2* light curve (red) based on a simple disc reprocessing. The normalization of the simulated light curve is arbitrary. The zero-point is the start of the intensive monitoring period.

The overall shapes of the two light curves are similar, with all of the large variations in the predicted model light curve having counterparts in the observed light curve, though the variations relative to the mean level are larger in the model light curve. As has been noted by a number of previous authors (e.g. Berkley et al. 2000; Arévalo et al. 2008), then for a lamp-post X-ray model, it is necessary to have a large X-ray source height (∼100 R_G) and a similarly large inner disc radius if the amplitude and degree of smoothness of the observed UV variability are to be reproduced, assuming that all of the reprocessing is carried out on an accretion disc. We confirm that, if all of the observed *UVW2* variability is to be produced by reprocessing of X-rays by just an accretion disc, then some blurring mechanism such as a large X-ray source height or scattering through the inner edge of the accretion disc (Gardner & Done 2017) would be needed to reproduce the observed *UVW2* amplitude of variability.

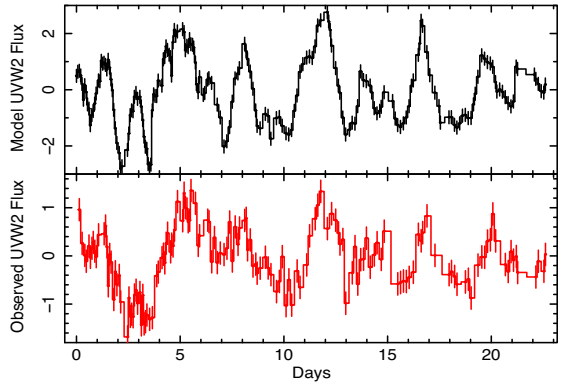

Figure 13. The model (upper panel) and observed (lower panel) *UVW2* light curves from Fig. 12 following subtraction of the mean level derived from smoothing with a 5 d wide boxcar.

There are differences between the observed and model light curves in the long-term variations, e.g. with the model light curve rising in the last 5 d of the observations whereas the observed light curve continues the decrease that has been going on for the previous ∼15 d. Although the peaks appear to line up reasonably well, JAVELIN gives a lag of the model *UVW2* by the observed *UVW2* of 0.62 ± 0.03 d, which is similar to the lag of the observed X-rays by the observed *UVW2*. The FR/RSS method gives a similar lag for the distribution of the centroids of the correlation functions of 0.55 ± 0.10 d, although a shorter lag (0.28 ± 0.12 d) for the distribution of the peaks of the correlation functions. The mean peak correlation coefficient is 0.74.

If we remove the mean level derived from smoothing with a boxcar, the similarity between the remaining observed and model light curves increases, e.g. in Fig. 13 where a boxcar of width 5 d has been used. A similar relationship between the X-ray and *UVW2* light curves was also seen in NGC 5548 after long time-scale variations had been removed (fig. 5 of McHardy et al. 2014). The similarity between the observed and model light curves indicates a strong causal relationship, as far as the short time-scale variability is concerned, between the driving X-ray light curve and the observed *UVW2* light curve. For the light curves shown in Fig. 13, the lag derived by JAVELIN is 0.20 ± 0.03 d and the FR/RSS mean centroid lag is to 0.13 ± 0.05 d. The lags decrease as the boxcar width is reduced. With data of very high time resolution and with very short autocorrelation time-scales it might be possible to distinguish separate peaks in cross-correlation functions. However, with most real data, including the present data, the peaks are blurred together and so the effect of adding a long time-scale lag to a short time-scale lag is actually to produce a correlation function with an intermediate lag.

These results show that there are longer time-scale variations in the observed *UVW2* light curve which are not reproduced by modelling by an accretion disc. However, the short time-scale (<5 d) variations can, at least to first order, be reproduced by reprocessing of the X-rays, or by some other high energy emission with similar variability properties to the X-rays, by an accretion disc. There is still some additional lag of the observed *UVW2* over and above that expected from reprocessing, but it is small, and decreases as lower frequency variations are filtered out. We note that the observed lag of the unfiltered X-rays by *UVW2* is ∼0.66d. This lag is much longer than might be explained by an X-ray source of size ∼100 R_G or a similarly large inner disc radius as, for NGC 4593, ∼100 R_G corresponds to 0.04d.

If the inflated inner edge of the accretion disc acts as a scatterer for the hard X-rays, adding an addition lag as in the model of Gardner & Done (2017), the fact that the X-ray to *UVW2* lag becomes smaller as we remove long time-scale variations may indicate a stratified scatterer. Thus, X-rays which scatter from the top of the inflated inner disc may only undergo a small number of scatterings. They would therefore not suffer a large additional delay beyond the light traveltime expected from direct illumination of the outer disc. Similarly, the reprocessed signal in the UVOT bands should not be greatly blurred. However, X-rays which travel through a greater path-length of scatterer, along the mid-plane of the disc, will suffer longer delays and will also result in a more blurred reprocessing signal. In this model, the total UVOT light curves should be a sum of all of the reprocessed contributions.

5.2 Energetics

We can make a rough determination of whether the X-rays could be directly powering the UV/optical variations by comparing the X-ray luminosity hitting the disc, for various source geometries, and the luminosity in the varying (not the steady) component of the UV/optical fluxes. The BAT 70 month survey gives an average 14–195 keV luminosity of 1.58×10^{43} erg s^{-1}. Extrapolating to 0.1–195 keV with $\Gamma = 1.75$ gives 3×10^{43} erg s^{-1} which we take as an approximate estimate of the total X-ray luminosity. As the lowest observed X-ray count rates are almost zero, we assume that all of the X-ray emission comes from the central varying compact source and that there is no significant quiescent component.

To estimate the total varying luminosity over the UVOT bands we have fitted models in XSPEC to the data shown in Fig. 11. The models are not well constrained but the total flux, $\sim 1.16 \times 10^{-11}$ erg cm^{-2} s^{-1} over the range covered by the UVOT (∼1850−5500 Å), does not vary by more than 10 per cent between models giving, for a distance of 35 Mpc, a luminosity of $\sim 1.7 \times 10^{42}$ erg s^{-1}.

To estimate the solid angle subtended at the X-ray source by the UV/optical emitting regions of the disc, we estimate, from Fig. 9, that the bulk of the UV and optical emission detected by the UVOT comes from between radii of 10–300 R_G (1 R_G = 38s). For an X-ray point source at a height, H, of 6 R_G, this range of the disc subtends 3.22 sr, i.e. a covering fraction of 0.257 (or 0.346 for $H = 10\ R_G$). Conservatively taking the lower figure gives an X-ray luminosity of 7.7×10^{42} erg s^{-1} impacting the UVOT-emitting part of the disc, i.e. about 4.5×the observed UVOT luminosity. Thus, even with a disc albedo of ∼80 per cent, there would be sufficient X-ray illumination to power the observed UV/optical emission.

As an alternative way of demonstrating the energetics we show, in Fig. 14 the broad-band SED. The exact model fit in the UVOT bands is not important but we can see that the total luminosity in the UVOT bands does not exceed that in one decade of the X-ray spectrum.

There are, of course, a number of uncertainties in this calculation, e.g. the albedo, the X-ray source size, the illuminating X-ray energy band and the inner radius of the emission region (the outer is relatively unimportant). We may also wish to consider the emission at shorter wavelengths than *UVW2*, but then we would have to also decrease the inner radius which would increase the solid angle. Here, we therefore conclude that, at least to first order, there is sufficient X-ray luminosity to power the observed UV/optical variations.

The above accretion disc modelling is quite basic, but serves to show that although reprocessing by an accretion disc can reproduce a good deal of the short time-scale UV variability, there are variations on longer time-scales, with larger lags, which cannot be

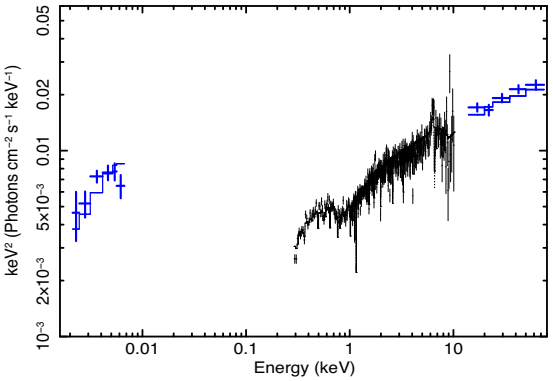

Figure 14. Broad-band $\nu F(\nu)$ SED of NGC 4593, including the variable UVOT components, fitted to the same model as in Fig. 2, together with a disc blackbody in the UVOT bands.

explained by reprocessing purely by an accretion disc. To explain all of the UV/optical variations by reprocessing of X-rays, we therefore require more than just an accretion disc as the reprocessor. Below we provide more sophisticated modelling to derive the reprocessing functions needed to reproduce all variations.

6 MEMECHO MODELLING OF X-RAYS DRIVING THE UV AND OPTICAL VARIATIONS

Visual inspection of the light curves and cross-correlation analysis indicates that a physical relationship exists between the X-ray variations and the UV/optical variations. In order to test the reality of this relationship, and to infer delay distributions rather than just mean lags for each of the UV/optical light curves, we here fit the light curves in detail, under the assumption that the X-ray variations are driving time-delayed responses in other bands.

We employed the maximum entropy fitting code MEMECHO (Horne 1994; Horne et al. 2004) to fit the *Swift* light-curve data with a *linearized* echo model

$$F(t|\lambda) = F_0(\lambda) + \int_0^{\tau_{\rm max}} \Psi(\tau|\lambda)\ (X(t-\tau) - X_0)\ {\rm d}\tau. \qquad (2)$$

Here $X(t)$ is the driving (X-ray) light curve. X_0 is an arbitrary reference level, set at the median of the X-ray data. $F_0(\lambda)$ is the corresponding reference level in the echo light curve and $\Psi(\tau|\lambda)$ is the delay map (i.e. the response function) for the echo response at wavelength λ.

Fig. 15 shows a MEMECHO fit to the *Swift* light-curve data, where $X(t)$ is adjusted to fit the X-ray (0.5–10 keV) light curve, and the reference levels $F_0(\lambda)$ and delay distributions $\Psi(\tau|\lambda)$ are adjusted to fit the three UV light curves (*UVW*2, *UVM*2, *UVW*1) and the three optical light curves (U, B, V).

MEMECHO adjusts the model X-ray light curve and the echo reference levels and delay maps to find a 'good' fit to all observed light curves, i.e. X-ray, UV, and optical, with a 'simple' model. The 'good' fit requirement is imposed on the model by requiring a specific value of χ^2/N, where $N = 1171$ is the number of data values. The competing requirement of a 'simple' model is achieved by maximizing the entropy S of the functions $X(t)$ and $\Psi(\tau|\lambda)$.

We sample $X(t)$ and $\Psi(\tau|\lambda)$ on uniform grids in t and τ, with the same fine spacing $\Delta t = 0.01$ d in order to resolve the most rapid structure in the X-ray light curve. We restrict the delay map to τ in the range 0–10 d, with $\tau > 0$ to impose causality (no UV/optical response prior to X-ray variations) and $\tau < 10$ d since this is roughly 1/3 of the timespan of the data and there is no sign, in the simple cross-correlations above of any strong correlation on time-scales greater than ∼2 d.

The entropy of the discretely sampled positive function, $p(t) = p_i$ at $t = t_i$, is defined as

$$S(p) = p_i - q_i - p_i\ \ln p_i/q_i, \qquad (3)$$

where for each p_i the default value q_i is the geometric mean of its neighbours, $q_i = (p_{i-1}\ p_{i+1})^{1/2}$. With this definition the entropy has a regularizing effect, expressing a preference for smooth positive functions, favouring Gaussian peaks and exponential tails. A parameter W scales the entropy weight of the echo delay maps relative to that of the X-ray light curve, controlling their relative flexibility.

In fitting the *Swift* light curves, we ran MEMECHO repeatedly to find a grid of models fitting the data with χ^2/N ranging from 2 to 0.8, and for $W = 1$ and 10. Here, the χ^2 level controls the trade-off between resolution and noise in the resulting delay maps. For higher χ^2, the model light curves are too smooth to follow significant features in the light-curve data. For lower χ^2 the model fits more subtle features in the light-curve data, but to do so the delay maps, and to a lesser extent the model X-ray light curve, develop larger amplitude fine-scale structure that eventually, for the smallest χ^2, becomes unacceptable.

Fig. 15 presents the MEMECHO fit for $\chi^2/N = 1.5$ and $W = 10$, which we judge by eye to achieve the right balance, giving a 'good' fit that is not excessively 'noisy'. Roughly speaking $W = 10$ allows the X-ray light curve $X(t)$ to be 10 times more flexible than the delay maps $\Psi(\tau|\lambda)$. This is appropriate since the most rapid structure in the X-ray light curve is not evident in the echo light curves.

Notice that the delay maps share a similar structure, with a prompt response peak at $\tau = 0$, roughly 1/4 of the response at $\tau < 1$ d, plus a broader response tail decreasing towards $\tau = 10$ d. The extended response is generally stronger at longer wavelengths. Small bumps and wiggles on the extended response do not show a clear trend with wavelength. These may be unreliable artefacts arising from attempts to fit the echo model to residual systematic errors in the light-curve data and/or to variations that are not driven by the X-ray variations.

The fitted model adequately represents most of the features in the light-curve data, consistent with the X-ray variations driving linear responses in the UV and optical light. Evidence for the prompt response peak at $0 < \tau < 1$ d arises from many X-ray features with well-detected counterparts in the echo light curves. For example, the three X-ray dips during 7583–7585 have corresponding dips in the UV echo light curves, as do the peaks at 7599 and 7602. The more extended response is needed to produce the gradual decrease in the echo light curves.

A few minor defects in the fit may also be noted. The 1-d X-ray dip at 7590 has no counterpart in the echo light curves. The 2-d peak near 7494 in the echo light curves is well modelled, but the corresponding X-ray feature is stronger than required, so that the model X-ray light curve falls below the X-ray data in this region. In particular, the fit inserts a narrow X-ray dip in a data gap near 7594.6.

To summarize, our main conclusion is that the linearized echo model provides an acceptable fit to the *Swift* light-curve data in all wavebands. We require that the delay structure has a prompt response peak with $0 < \tau < 1$ d to produce rapid correlated variations on 1-d time-scales while washing out, from the UV/optical light curves, sub-day structure seen in the X-ray light curve. We also require an extended tail to the delay structures to produce a gradual decline in the UV/optical echo light curves. The rapid response

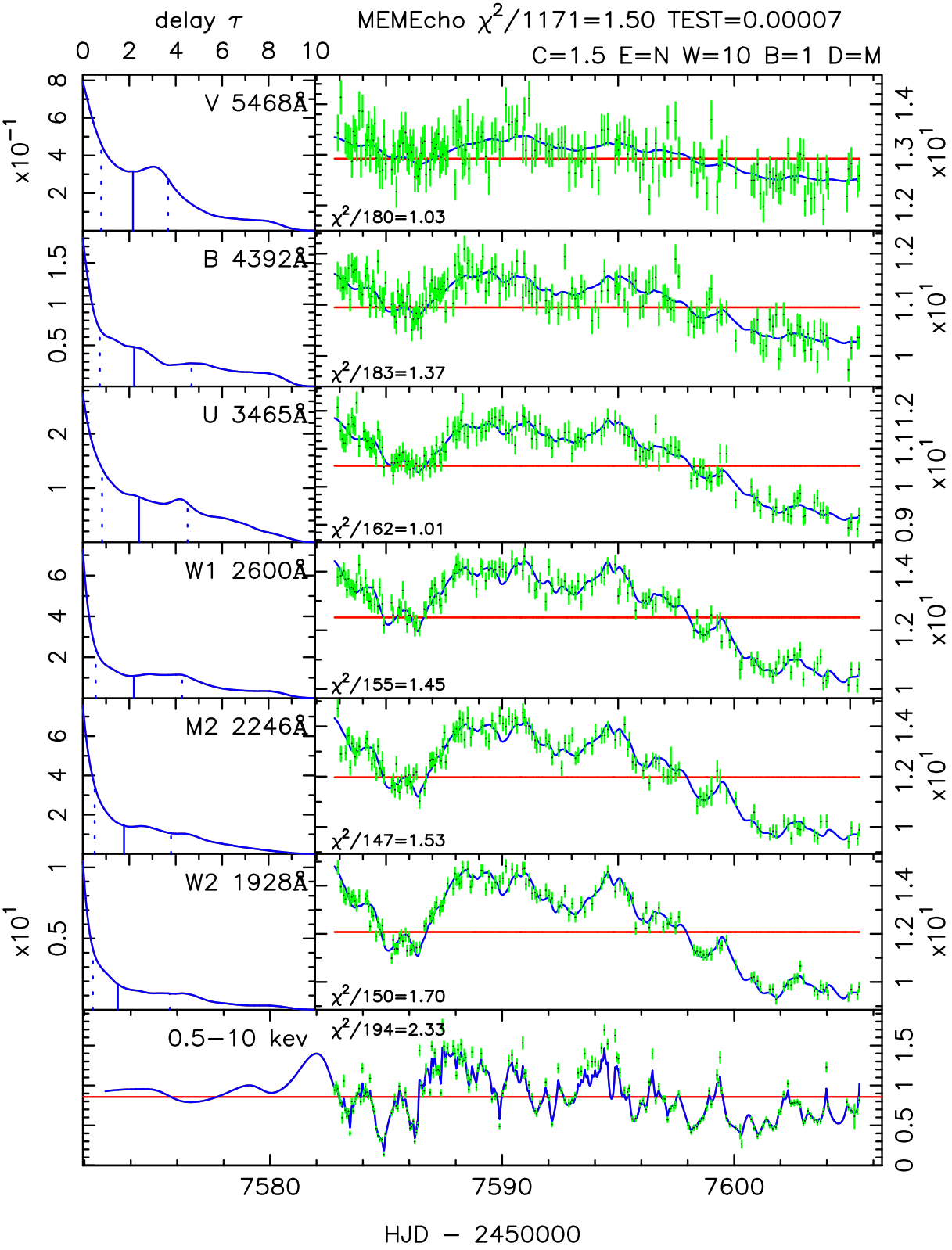

Figure 15. MEMECHO fit of the linearized echo model to *Swift* light urves of NGC 4593. *Bottom panel:* X-ray (0.5–10 keV) light-curve data along with the fitted model $X(t)$. *Left column:* Delay distributions $\Psi(\tau|\lambda)$ for three UV (*UVW*2, *UVM*2, *UVW*1) and three optical (*U*, *B*, *V*) bandpasses. *Right column: Swift* light-curve data along with the echo light curves obtained by convolving $X(t)$ with $\Psi(\tau|\lambda)$. Vertical (blue) lines indicate the median (solid) and quartiles (dashed) of the delay distributions. Horizontal (red) lines indicate the reference levels X_0 for the X-ray light curve and $F_0(\lambda)$ for the echo light curves. The fit shown is for $\chi^2/N = 1.5$ with $W = 10$ to make $X(t)$ 10 times more flexible than $\Psi(\tau|\lambda)$. Note the two-component structure of the delay maps, with a prompt response peak at $\tau = 0$ and extended response reaching to $\tau = 10$ d.

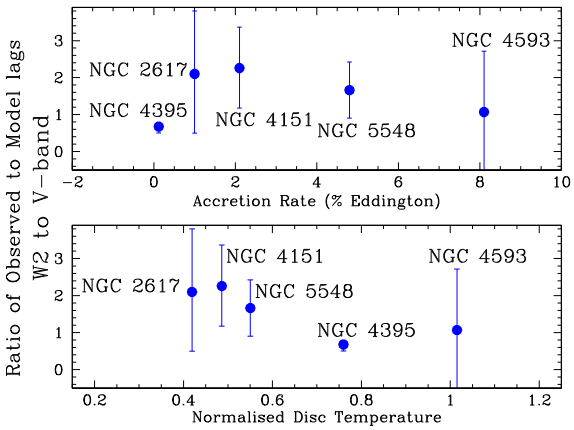

Figure 16. The ratio of observed to model lags for the *W*2 to *V*- band lag. In the upper panel the ratio is plotted as a function of accretion rate and in the lower panel as a function of normalized disc temperature, i.e. $(\dot{m}_E/M)^{1/4}$. The model assumes reprocessing of X-rays by a standard optically thick accretion disc (Shakura & Sunyaev 1973). The data from which this plot is produced are given in Table 3.

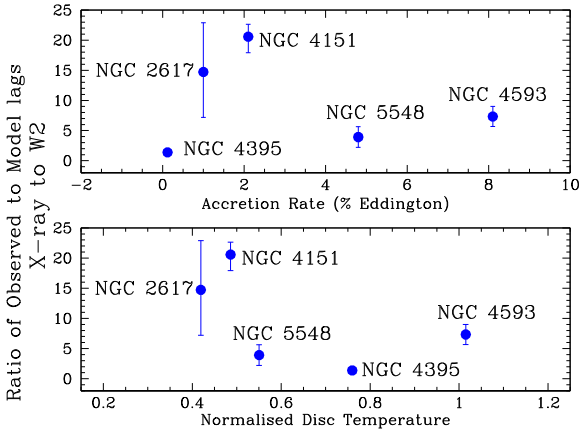

Figure 17. As for Fig. 16 except that the ratio of observed to model lags is for the X-ray to *W*2-band lag.

would naturally be produced by reprocessing on a nearby accretion disc with the more extended response being produced in the BLR gas. This latter possibility is discussed in more detail in Cackett et al. (2018).

7 DISCUSSION

7.1 Comparison of AGN lag spectra: cosmological standard measuring rods?

7.1.1 UVW2 to V-band lags

Well-measured X-ray/UV/optical lags as measured by *Swift* have already been published for NGC 2617 (Shappee et al. 2014; Fausnaugh et al. 2018), NGC 4151 (Edelson et al. 2017), and NGC 5548 (McHardy et al. 2014; Edelson et al. 2015) and well-measured lags between the X-ray and *UVW*1 from *XMM–Newton* and ground-based *g* bands in NGC 4395 have also been published (McHardy et al. 2016). These observed lags, together with the observed lag measured here for NGC 4593, together with model lags assuming reprocessing on an accretion disc, using the model code from which the response functions given above (Fig. 9), are given in Table 3. Here, as the 'observed' lags, we simply use the measured lags between the *UVW*2 and *V* bands. One might define the lag in other ways, e.g. from a fit to the overall lag spectrum. Such a method would produce a smaller uncertainty. However, such fits involve assumptions, e.g. about which bands to include and so, for the present, we use the simple measured lag between the two bands.

To determine whether the ratio of observed to model lags varies between AGN, or depends on particular AGN parameters, we present, in Fig. 16 the ratio of the observed to model lags as a function of both accretion rate and normalized disc temperature [i.e. $(\dot{m}_E/M)^{1/4}$]. A constant is a good fit to these data. A slight decrease of the ratio with increasing accretion rate would also be an acceptable fit, except for NGC 4395. However, NGC 4395 has a much lower mass than the other 4 AGN. If we plot the ratios against disc temperature, which takes account of mass and is arguably a more relevant parameter for describing disc structure than simple accretion rate, then NGC 4395 is not an outlier to a very slight decreasing trend. However, better data are required before any such trend can be claimed.

The ratio of $\lesssim 2$ is consistent with the factor of 2.25 which we measured in NGC 5548 in McHardy et al. (2014) and with the factor $\sim 2-3$ which was quoted by subsequent RM programmes (e.g. Edelson et al. 2015; Fausnaugh et al. 2016; Edelson et al. 2017; Fausnaugh et al. 2018). Microlensing observations (e.g. Dai et al. 2010; Morgan et al. 2010; Mosquera et al. 2013) typically quote a somewhat larger ratio, $\sim 4\times$, but the methods used to measure the ratio are quite different.

We note that the deduced discrepancy between observed and model disc sizes may appear slightly different from one set of observations to another. For example, in NGC 5548 the *UVW*2 to *V*-band lag from McHardy et al. (2014) is $1.35^{+0.33}_{-0.35}$ d but from Edelson et al. (2015) is it 1.16 ± 0.53 d, although these lags are perfectly consistent within the errors. We also note that the model lags used here are based on the time for half of the reprocessed light to appear, as derived from a numerical computer model of the disc, rather than on an analytical calculation, which may have different assumptions, e.g. the value of the '*X*' parameter in equation 9 of Fausnaugh et al. (2016). However, perhaps most importantly, the wavelength range over which the comparison between model and observation is carried out can have a big effect on the deduced discrepancy (e.g. see Fausnaugh et al. 2016) as the observed lags in the different wavebands do not generally all lie smoothly on the same curve. The accompanying paper based on *HST* observations (Cackett et al. 2018) includes lags from both shorter and longer wavelengths than those used here and the inclusion of those additional lags leads to almost twice as large a discrepancy, assuming the analytic model predictions of Fausnaugh et al. (2016), than if just the *Swift* lags are used.

However, even given the above caveats, the general result that the observed lags between the optical and UV bands are within a factor of 2 to 3 of the model lags expected just from reprocessing of high energy radiation by a standard Shakura–Sunyaev accretion disc still holds. Moreover, apart possibly from a slight decrease of the ratio of observed to model lags with increasing disc temperature, there is very little difference between different AGN.

7.1.2 X-ray to UVW2 lags

The ratios of observed to model lags for the X-ray to *UVW*2 bands are, with the exception of NGC 4395, far from the expectations of a

standard accretion disc and also vary considerably from one AGN to another. The two lowest disc temperature AGN, NGC 2617, and NGC 4151 have the largest ratios but there is no simple relationship which will fit these data, either as a function of accretion rate or disc temperature. NGC 2617 (e.g. Giustini et al. 2017) and NGC 4151 (e.g. Keck et al. 2015; Beuchert et al. 2017) also have the largest neutral absorbing columns, both above 10^{23} cm^{-2}, in previous observations of this small sample but again there is no simple relationship between absorbing columns, either cold or warm, and the ratios discussed here. Further work, e.g. to measure the spectral absorption parameters from the same observations from which the lags were measured, is required to determine whether there is any relationship between absorbing columns and lag ratios.

The above results indicate that the *UVW*2 to *V*-band lags might be useful as a cosmological standard measuring rod (cf. Cackett et al. 2007) but any lags relative to the X-ray band must be treated with great care.

7.2 Geometry of the inner region: an extended reprocessor

The lags measured from unfiltered light curves show, in all cases, that the lags of all of the other UV/optical bands (except *U* band) relative to *UVW*2 are close to the predictions from the accretion disc model of Shakura & Sunyaev (1973) but the lag of the X-rays by the *UVW*2 band are much larger than predicted. Gardner & Done (2017) propose that the X-rays do not directly illuminate the outer accretion disc but instead heat up the inner accretion disc which re-radiates on to the disc in the far-UV. The additional lag between the X-ray and *UVW*2 bands is then the thermal time-scale for the X-rays to heat the inner disc. There are a number of attractive aspects of this model. The large far-UV emission region helps to smooth out the rapid variations in the X-ray band which would otherwise predict more rapid variations in the UV and optical bands than are observed. If the inner disc is very inflated by the X-ray heating, then the additional height of the emission region increases the solid angle subtended by the outer disc, thereby ensuring that there is adequate luminosity impacting on the outer disc to account for the observed UV and optical variations. A large far-UV emission region might be expected to have a tail of emission extending into the soft X-ray band. A weak soft excess has been seen by previous observers (e.g. Brenneman et al. 2007) but we do not find such a component in the present *Swift* data.

Here, we have shown here that when the X-ray and UV light curves are filtered to remove long time-scale variations, the X-ray to *UVW*2 lag becomes close to the predictions of disc reprocessing. A similar conclusion was reached regarding the lags in NGC 5548 by M$^{\rm c}$Hardy et al. (2014) and, for NGC 4395 whose lags were measured using *XMM–Newton* (M$^{\rm c}$Hardy et al. 2016) and therefore long time-scale variations were not measured, the lag ratio is very close to the expectations of disc reprocessing. These results show that although short time-scale UV/optical variability is consistent with X-ray reprocessing on a disc, there are longer time-scale variations in the UV and optical wavebands than cannot be accounted for by simple reprocessing of X-rays by an accretion disc. With MEMECHO analysis we have shown here that the X-rays can be a reasonable driver of the unfiltered variations in all bands as long as we allow for a complex reprocessor where, in addition to a close reprocessor such as the accretion disc, the reprocessing material extends to distances of a few light days from the illuminating source. The broad line region gas thus provides a natural explanation for the extended reprocessing region. This conclusion is consistent with the large excess lag seen in the *U* band which is almost certainly Balmer continuum emission resulting from reprocessing of high energy emission in the BLR (Korista & Goad 2001). We incidentally note that the excess *U*-band lag in NGC 4593 is larger than in the lower accretion rate AGN NGC 5548 and NGC 4151 where the inner edge of the BLR will be closer to the black hole. Although the data at present do not allow detailed analysis it might be interesting in future to see whether the *U*-band excess lag does vary with accretion rate.

The geometry of the BLR is not well known but it is likely to subtend a large solid angle at the X-ray source. Thus, worries concerning whether sufficient X-ray illumination hits the reprocessing to account for the resultant UV/optical emission are diminished. If we consider only the variable part of the UV/optical emission, the simple energetic arguments outlined above indicate that, although there is no great excess, there is probably enough X-ray illumination of the accretion disc to account for the observed short time-scale variability.

8 CONCLUSION

Although Starkey et al. (2017) find that the multiband observations of NGC 5548 cannot be satisfactorily accounted for simply by reprocessing of X-rays, the *Swift* UV/optical light curves of NGC 4593 can be reasonably reproduced by reprocessing of X-rays, but by a complex reprocessor including a nearby accretion disc and more distant broad line gas clouds.

The observation of a large additional lag between the X-ray and *UVW*2 bands in all well-studied AGN, above the expectation of simple reprocessing from a nearby accretion disc, is at first sight good evidence for scattering of X-rays in the inner accretion disc. However, the measured additional lag becomes closer to the prediction of direct disc reprocessing both here in NGC 4593 and also in NGC 5548 (M$^{\rm c}$Hardy et al. 2014) as one filters out long time-scale variations, which may come from the broad line region gas. In the case of multiple or extended reprocessors then, in perfect data, we would be able to detect separate peaks corresponding to different lags in the cross-correlation function. However, with the present data, the effect is to produce asymmetric correlation functions where the peak is some combination of the individual contributing lags. Thus, reprocessing in the BLR may explain at least part of the additional X-ray/*UVW*2 lag.

It is not known how the UVOT spectrum extrapolates to shorter wavelengths. Thus, we do not know how much reprocessed emission we need to produce. However, there appears to be enough energy in the X-ray band to account, by direct illumination, for the variable part of the UVOT emission, assuming a 'standard' X-ray source of size $10R_G$.

There remains slight uncertainty regarding the amplitude of variability of the reprocessed *UVW*2 emission. Simple reprocessing of the observed X-ray light curve only from an accretion disc produces larger amplitude *UVW*2 variability than is observed. However, MEMECHO analysis of reprocessing from an extended reprocessor can reproduce a model *UVW*2 light curve which is an acceptable fit to the observed light curve. The only caveat here is that the input X-ray light curve is not the directly observed light curve but is a fit to the X-ray light curve. However it is a reasonable fit, i.e. a reasonable description of the underlying light curve, given the noise involved in all observational measurements.

For the small number of AGN monitored so far, the UV/optical lags scale broadly similarly with mass and accretion rate, typically being a factor $\lesssim 2$ of the expectations from disc reprocessing for the *UVW*2 to *V*-band lag. The ratio of observed to model lags is in good

agreement with being constant, but is also in agreement with a slight decrease in observed/model ratio with increasing disc temperature. Such a decrease would be consistent with a more stable disc at higher temperatures (Churazov, Gilfanov & Revnivtsev 2001) as a less stable disc may be more clumpy (Dexter & Agol 2011) and hence radiate more at larger radii and so appear larger.

The X-ray to *UVW2* lags, however, are all larger than the expectations from disc reprocessing, and the discrepancy varies between AGN. However, although the largest discrepancy occurs in the two AGN (NGC 2617 and NGC 4151) which have both the largest cold absorbing columns and the coolest discs, there is no clear relationship between accretion rate, disc temperature, or absorbing column, cold or warm, and the size of the observed to model lag ratio for the X-ray to *UVW2* lags.

ACKNOWLEDGEMENTS

This paper is dedicated to the memory of Neil Gehrels. Without his inspired leadership of the Swift mission the research presented here, and in other similar AGN monitoring programmes, would not have been possible. IMM acknowledges support from a Royal Society Leverhulme Trust Research Fellowship LT160006 and from Science and Technology Facilities Council (STFC) grant ST/M001326/1. KH acknowledges support from STFC grant ST/M001296/1 and JG acknowledges support from the US National Aeronautics and Space Administration (NASA) under awards NNX15AH49G and 80NSSC17K0126. MV acknowledges financial support from the Danish Council for Independent Research via grant DFF 4002-00275. MP acknowledges support from a Royal Society Science and Engineering Research Board Newton International Fellowship. This work made use of data supplied by the UK Swift Science Data Centre at the University of Leicester.

REFERENCES

Alexander T., 2013, preprint (arXiv:1302.1508)
Arévalo P., Uttley P., 2006, MNRAS, 367, 801
Arévalo P., Uttley P., Kaspi S., Breedt E., Lira P., McHardy I. M., 2008, MNRAS, 389, 1479
Arévalo P., Uttley P., Lira P., Breedt E., McHardy I. M., Churazov E., 2009, MNRAS, 397, 2004
Baumgartner W. H., Tueller J., Markwardt C. B., Skinner G. K., Barthelmy S., Mushotzky R. F., Evans P. A., Gehrels N., 2013, ApJS, 207, 19
Bentz M. C., Katz S., 2015, PASP, 127, 67
Berkley A. J., Kazanas D., Ozik J., 2000, ApJ, 535, 712
Beuchert T. et al., 2017, A&A, 603, A50
Blandford R. D., M cKee C. F.c, 1982, ApJ, 255, 419
Breedt E. et al., 2009, MNRAS, 394, 427
Breedt E. et al., 2010, MNRAS, 403, 605
Brenneman L. W., Reynolds C. S., Wilms J., Kaiser M. E., 2007, ApJ, 666, 817
Burrows D. N. et al., 2005, Space Sci. Rev., 120, 165
Cackett E. M., Horne K., Winkler H., 2007, MNRAS, 380, 669
Cackett E. M., Zoghbi A., Reynolds C., Fabian A. C., Kara E., Uttley P., Wilkins D. R., 2014, MNRAS, 438, 2980
Cackett E. M., Chiang C.-Y., McHardy I. M., Edelson R., Goad M. R., Horne K., Korista K. T., 2018, ApJ, 857, 53
Cameron D. T., McHardy I. M., Dwelly T., Breedt E., Uttley P., Lira P., Arevalo P., 2012, MNRAS, 422, 902
Churazov E., Gilfanov M., Revnivtsev M., 2001, MNRAS, 321, 759
Connolly S., 2015, preprint (arXiv:1503.06676)
Connolly S. D., McHardy I. M., Dwelly T., 2014, MNRAS, 440, 3503
Dai X., Kochanek C. S., Chartas G., Kozłowski S., Morgan C. W., Garmire G., Agol E., 2010, ApJ, 709, 278
Dexter J., Agol E., 2011, ApJ, 727, L24
Edelson R. A., Krolik J. H., 1988, ApJ, 333, 646
Edelson R. et al., 2015, ApJ, 806, 129
Edelson R. et al., 2017, ApJ, 840, 41
Emmanoulopoulos D., McHardy I. M., Papadakis I. E., 2013, MNRAS, 433, 907
Emmanoulopoulos D., Papadakis I. E., Dovčiak M., McHardy I. M., 2014, MNRAS, 439, 3931
Evans P. A. et al., 2007, A&A, 469, 379
Fausnaugh M. M. et al., 2016, ApJ, 821, 56
Fausnaugh M. M. et al., 2018, ApJ, 854, 107
Gardner E., Done C., 2017, MNRAS, 470, 3591
Gaskell C. M., 2008, Rev. Mex. Astron. Astrofis. Conf. Ser., 32, 1
Gaskell C. M., Peterson B. M., 1987, ApJS, 65, 1
Gaskell C. M., Sparke L. S., 1986, ApJ, 305, 175
Gelbord J., Edelson R., 2017, AAS/High Energy Astrophysics Division, Meeting 16, p. 113.05
Giustini M. et al., 2017, A&A, 597, A66
Haardt F., Maraschi L., 1991, ApJ, 380, L51
Horne K., 1994, in Gondhalekar P. M., Horne K., Peterson B. M., eds, ASP Conf. Ser. Vol. 69, Reverberation Mapping of the Broad-Line Region in Active Galactic Nuclei. Astron. Soc. Pac., San Francisco, p. 23
Horne K., Peterson B. M., Collier S. J., Netzer H., 2004, PASP, 116, 465
Kazanas D., Nayakshin S., 2001, ApJ, 550, 655
Keck M. L. et al., 2015, ApJ, 806, 149
Korista K. T., Goad M. R., 2001, ApJ, 553, 695
Lira P., Arévalo P., Uttley P., McHardy I. M., Breedt E., 2011, MNRAS, 415, 1290
McHardy I. M., Papadakis I. E., Uttley P., Page M. J., Mason K. O., 2004, MNRAS, 348, 783
McHardy I. M. et al., 2014, MNRAS, 444, 1469
McHardy I. M. et al., 2016, Astron. Nachr., 337, 500
Morgan C. W., Kochanek C. S., Morgan N. D., Falco E. E., 2010, ApJ, 712, 1129
Mosquera A. M., Kochanek C. S., Chen B., Dai X., Blackburne J. A., Chartas G., 2013, ApJ, 769, 53
Nandra K., Clavel J., Edelson R. A., George I. M., Malkan M. A., Mushotzky R. F., Peterson B. M., Turner T. J., 1998, ApJ, 505, 594
Oknyanskii V. L., 1993, Astron. Lett., 19, 416
Oknyansky V. L. et al., 2017, MNRAS, 467, 1496
Pal M., Naik S., 2018, MNRAS, 474, 5351
Pancoast A., Brewer B. J., Treu T., 2014, MNRAS, 445, 3055
Peterson B. M., 2014, Space Sci. Rev., 183, 253
Peterson B. M., Wanders I., Horne K., Collier S., Alexander T., Kaspi S., Maoz D., 1998, PASP, 110, 660
Peterson B. M. et al., 2005, ApJ, 632, 799
Roming P. W. A. et al., 2005, Space Sci. Rev., 120, 95
Sergeev S. G., Doroshenko V. T., Golubinskiy Y. V., Merkulova N. I., Sergeeva E. A., 2006, in Gaskell C. M., McHardy I. M., Peterson B. M., Sergeev S. G., eds, ASP Conf. Ser. Vol. 360, AGN Variability from X-Rays to Radio Waves. Astron. Soc. Pac., San Francisco, p. 13
Shakura N. I., Sunyaev R. A., 1973, A&A, 24, 337
Shappee B. J. et al., 2014, ApJ, 788, 48
Sobolewska M. A., Papadakis I. E., 2009, MNRAS, 399, 1597
Starkey D. et al., 2017, ApJ, 835, 65
Suganuma M. et al., 2006, ApJ, 639, 46
Summons D. P., 2007, PhD thesis, University of Southampton
Taylor R. D., Uttley P., McHardy I. M., 2003, MNRAS, 342, L31
Timmer J., Koenig M., 1995, A&A, 300, 707
Troyer J., Starkey D., Cackett E. M., Bentz M. C., Goad M. R., Horne K., Seals J. E., 2016, MNRAS, 456, 4040
Ursini F. et al., 2016a, Astron. Nachr., 337, 552
Ursini F. et al., 2016b, MNRAS, 463, 382
Uttley P., Edelson R., McHardy I. M., Peterson B. M., Markowitz A., 2003, ApJ, 584, L53
Vasudevan R. V., Fabian A. C., 2009, MNRAS, 392, 1124
Vasudevan R. V., Mushotzky R. F., Winter L. M., Fabian A. C., 2009, MNRAS, 399, 1553

Vasudevan R. V., Fabian A. C., Gandhi P., Winter L. M., Mushotzky R. F., 2010, MNRAS, 402, 1081
Woo J.-H., Urry C. M., 2002, ApJ, 579, 530
Zu Y., Kochanek C. S., Peterson B. M., 2011, ApJ, 735, 80
Zu Y., Kochanek C. S., Kozłowski S., Udalski A., 2013, ApJ, 765, 106

[1]*Department of Physics and Astronomy, The University of Southampton, Southampton SO17 1BJ, UK*
[2]*SUPA Physics and Astronomy, University of St. Andrews, North Haugh KY16 9SS, UK*
[3]*Department of Physics and Astronomy, Wayne State University, 666 W. Hancock Street, Detroit, MI 48201, USA*
[4]*Spectral Sciences Inc, 4 Fourth Avenue, Burlington, MA 01803, USA*
[5]*Department of Astronomy, The Ohio State University, 140 W 18th Avenue, Columbus, OH 43210, USA*
[6]*Space Telescope Science Institute, 3700 San Martin Drive, Baltimore, MD 21218, USA*
[7]*Inter-University Centre for Astronomy and Astrophysics, Pune 411007, India*
[8]*Astrophysics Science Division, NASA Goddard Space Flight Center, Greenbelt, MD 20771, USA*
[9]*Department of Physics and Astronomy, University of Leicester, Leicester LE1 7RH, UK*
[10]*Departamento de Astronomia, Universidad de Chile, Camino del Observatorio 1515, Santiago, Chile*
[11]*Facultad de Ciencias, Instituto de Fsica y Astronoma, Universidad de Valparaíso, Gran Bretana N 1111, Playa Ancha, Valparaso, Chile*
[12]*Department of Astronomy and Astrophysics, Pennsylvania State University, 525 Davey Laboratory, University Park, PA 16802, USA*
[13]*Institute of Astronomy, University of Cambridge, Madingley Road, Cambridge CB3 0HA, UK*
[14]*Aryabhatta Research Institute of Observational Sciences (ARIES), Manora Peak, Nainital 263002, India*
[15]*Department of Physics, University of Durham, South Road, Durham DH1 3LE, UK*
[16]*Harvard-Smithsonian Center for Astrophysics, Cambridge, MA 02138, USA*
[17]*School of Physics and Astronomy, Raymond and Beverly Sackler Faculty of Exact Sciences, Tel Aviv University, Tel Aviv 69978, Israel*
[18]*Department of Physics, Western Michigan University, 1120 Everett Tower, Kalamazoo, MI 49008-5252, USA*
[19]*Department of Physics, Institute of Theoretical and Computational Physics, University of Crete, 71003 Heraklion, Greece*
[20]*Department of Astrophysics and Astronomy, Tata Institute of Fundamental Research, Mumbai 40005, India*
[21]*Astronomical Institute 'Anton Pannekoek,' University of Amsterdam, Postbus 94249, NL-1090 GE Amsterdam, the Netherlands*
[22]*Dark Cosmology Centre, Niels Bohr Institute, University of Copenhagen, Juliane Maries Vej 30, DK-2100 Copenhagen, Denmark*
[23]*Steward Observatory and Department of Astronomy, University of Arizona, 933 N Cherry Avenue, Tucson, AZ 85721, USA*

This paper has been typeset from a TEX/LATEX file prepared by the author.